Journal of Molecular Structure 1343 (2025) 142824

Contents lists available at ScienceDirect

Journal of Molecular Structure

journal homepage: www.elsevier.com/locate/molstr

Eco-friendly sustainable synthesis of 2-phenoxy schiff bases supported on $SO_4^{2-} - TiO_2$: a comprehensive study of structure and antimicrobial activity

N. Dinesh kumar [a], S. Rajmohan [b], K. Selvakumar [c], D. Rajamanickam [d], G. Thirunarayanan [e,*], M. Swaminathan [a,*]

[a] Nanomaterials Laboratory, Department of Chemistry, Kalasalingam Academy of Research and Education, Krishnankoil, India
[b] Department of Chemical Engineering, National Institute of Technology Warangal, Telangana 506004, India
[c] Department of Physiology, Saveetha Dental College and Hospitals, Saveetha Institute of Medical and Technical Science (SIMATS), Saveetha University, Chennai, 600 077, Tamil Nadu, India
[d] Department of Chemistry, Centre for Research and Development, Vinayaka Mission's Kirupananda Variyar Engineering College, Vinayaka Mission's Research Foundation (DU), Salem 636 308, Tamil Nadu, India
[e] Department of Chemistry, Annamalai University, Annamalainagar, 608 002, India

ARTICLE INFO

Keywords:
Sulfated-titania catalyst
Green synthesis
DFT
Antimicrobial assessment
In-silico studies

ABSTRACT

In this study, sulfated-titania (SO_4^{2-}-TiO_2) was employed as a sustainable, green catalyst to synthesize a series of novel phenoxy Schiff bases (**3a-3g**) through a microwave-assisted, solvent-free green protocol involving 2-phenoxyaniline and various aromatic aldehydes, achieving yields of 90–99 % within 4 min. The catalyst has been studied by FT-IR, powder X-ray diffraction, and SEM with EDS. The structures of the synthesized Schiff's bases (SBs) were elucidated through physicochemical and spectroscopic analyses like FT-IR, ^{1}H & ^{13}C NMR, and SC-X ray diffraction. Specifically, compounds **3d** and **3g** exhibited crystalline structures in the monoclinic and orthorhombic systems, respectively, with space groups denoted as C-1c and P-2_1. In-depth understanding of the synthesized SBs in their gaseous state, computational investigations encompassing molecular orbitals, chemical reactivity, stability, and molecular electrostatic potential are essential. Furthermore, antimicrobial assessment highlighted the effectiveness of the SBs toward a variety of gram-negative and gram-positive strains of bacteria, as well as fungal strains. Molecular docking studies employing AutoDock revealed notable binding interactions, with the most favourable binding energy of -7.22 kcal/mol observed in association with the Human Carbonyl Reductase (4Z3D) protein. In addition, *in silico* ADMET prediction showed enhanced pharmacokinetic profiles and reduced acute oral toxicity.

1. Introduction

Researchers in synthetic organic chemistry play critical roles in the identification and fabrication of novel molecules with broad applications in biological, pharmaceutical, and material chemistry. However, traditional technologies frequently fall short of environmental sustainability due to the production of undesirable byproducts and the excessive use of organic solvents [1]. Green synthesis is widely pursued to develop sustainable, environmentally friendly, and enduring methods. Following the principles of green chemistry, an effective green catalyst possessing essential attributes such as low cost, high stability, excellent selectivity, reusability, and significant reactivity is required to ensure both efficiency and eco-friendliness [2,3]. In recent years, significant effort has been dedicated to finding catalysts that streamline synthesis, preserve energy, and reduce environmental effects. Traditional organic catalysts frequently cause environmental problems, forcing the hunt for alternatives. Heterogeneous catalysts have evolved as a more sustainable alternative to homogeneous catalysts. Solid-supported reagents, especially nanocatalysts, have received a lot of interest over the past two decades. Catalysts supported on solid surfaces have higher activity and selectivity than isolated catalysts due to the larger effective surface area. Nanocatalysts are diverse reagents that may be easily synthesized and used in a variety of chemical reactions. They provide stability, cost-effectiveness, experimental ease, and safety. Moreover, solid-supported nanocatalysts have an environmental advantage since the catalysts can be efficiently recovered and reused via simple

* Corresponding authors.
E-mail addresses: drgtnarayanan@gmail.com (G. Thirunarayanan), m.swaminathan@klu.ac.in (M. Swaminathan).

https://doi.org/10.1016/j.molstruc.2025.142824
Received 4 February 2025; Received in revised form 29 April 2025; Accepted 27 May 2025
Available online 28 May 2025

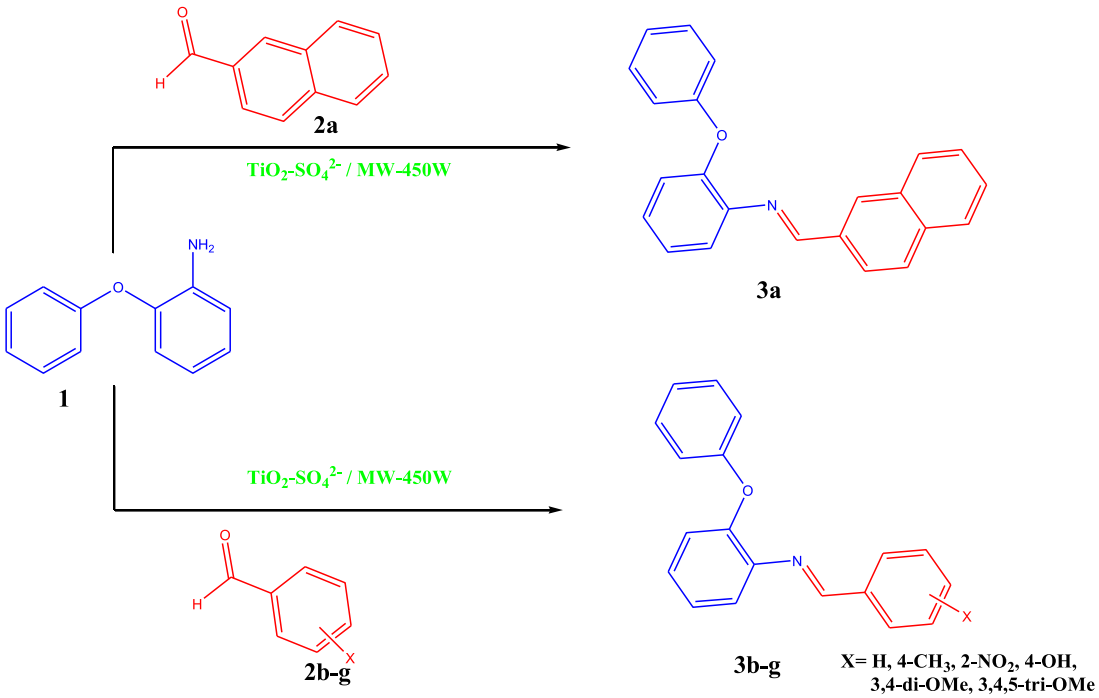

Scheme 1.. Synthesis of 2-phenoxy phenyl Schiff's bases (**3a-3g**).

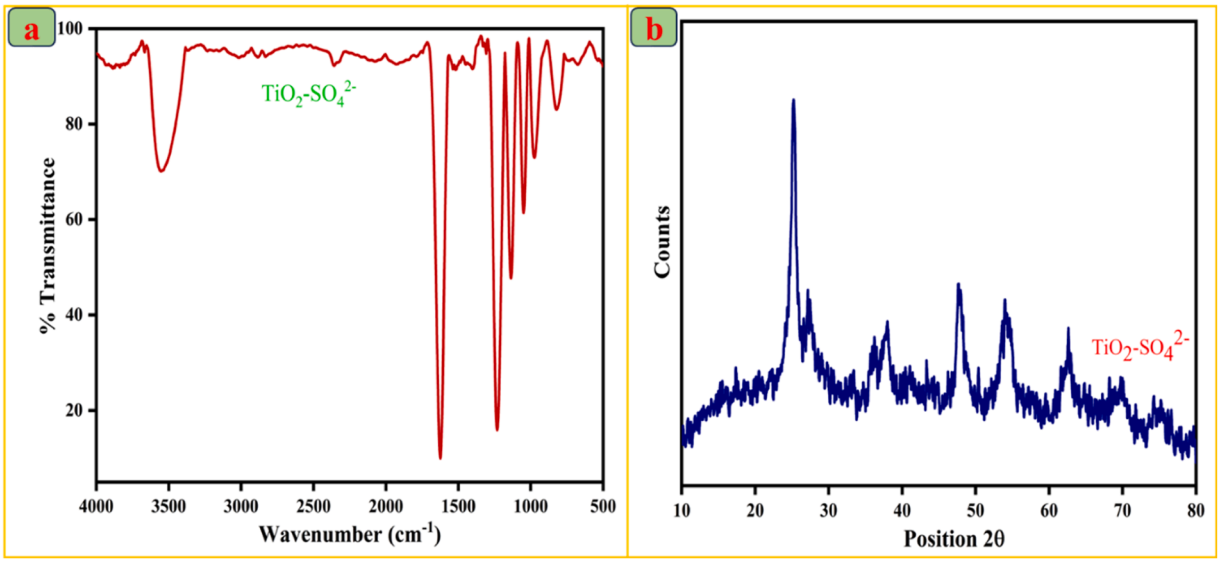

Fig. 1. FT-IR Spectrum (a) XRD pattern (b) of SO_4^{2-}-TiO_2.

filtration. Metal nanoparticles, in particular, feature a high surface-to-volume ratio, which results in more active sites per unit area than typical catalysts [4–7]. A variety of catalytic techniques employing transition metals such as copper, nickel, silver, zinc, gold, and titanium have been developed to enhance ecologically benign coupling reactions. Among these, titanium dioxide nanoparticles (TiO_2—NPs) have shown outstanding efficiency in aiding several cross-coupling reactions, including C—C, C—N, and C—O couplings, as well as cyclization reactions [8]. Mineral acids like H_2SO_4, HCl, and HF are commonly used as catalysts in a variety of industrial processes due to their high catalytic effectiveness. However, their utilization raises significant concerns, such as severe environmental pollution, high energy needs, separation and recovery issues, and equipment corrosion. For example, the industrial use of H_2SO_4 alone produces over 15 million tons of non-recyclable trash annually [9–11]. To overcome these challenges, recyclable solid acid catalysts, such as sulfated titanium dioxide (SO_4^{2-}-TiO_2), have emerged as possible solutions. Incorporating sulfate ions (SO_4^{2-}) improves the Brønsted and Lewis acidity of TiO_2, mimicking the catalytic activity of classic mineral acids while being eco-friendly and recyclable. These improvements make SO_4^{2-}-TiO_2 extremely effective for a variety of acid-catalyzed reactions [12,13]. Nevertheless, achieving stability, cost-effectiveness, and performance comparable to H_2SO_4 in large-scale industrial uses remains a critical issue.

The SBs are a major class of organic compounds that have been extensively researched due to their multifunctional characteristics. These compounds are formed through the condensation of amino molecules like NH_2, NH_2OH, or NH_2–NH_2 with carbonyl groups of aldehydes or ketones. These compounds, discovered in 1864 by German scientist

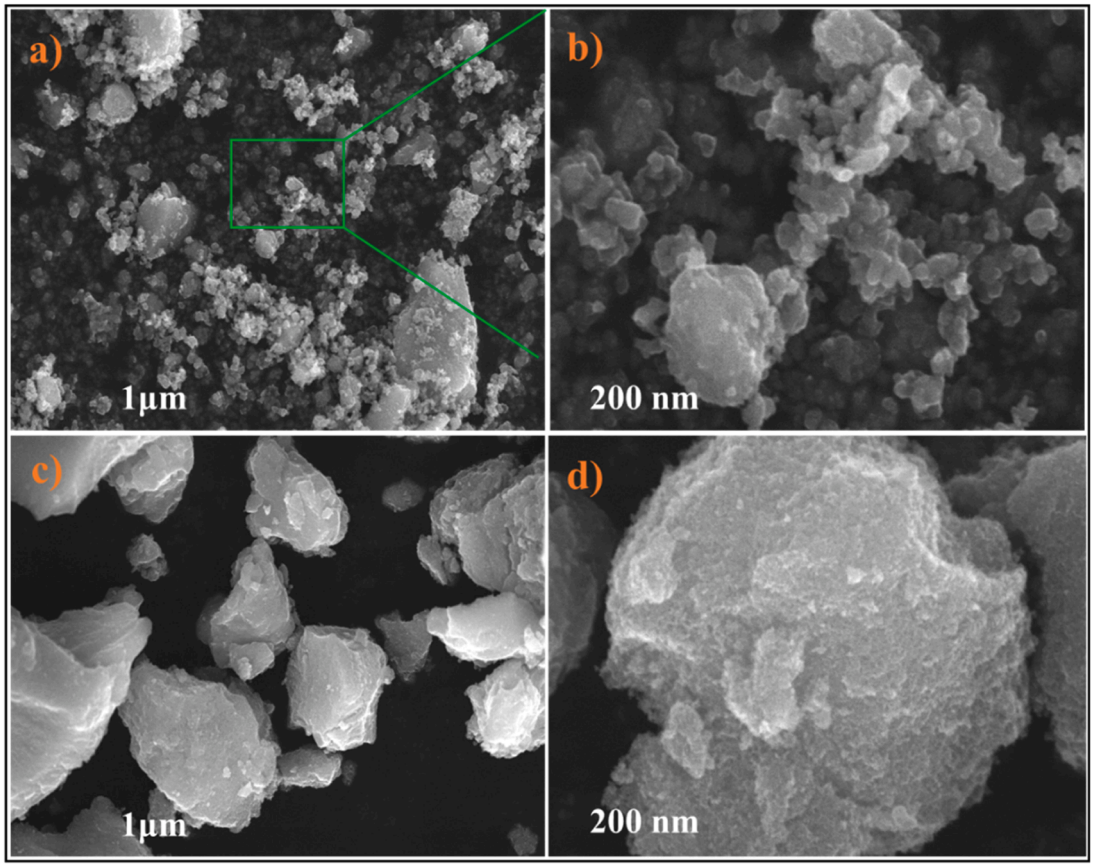

Fig. 2.. SEM images of SO_4^{2-}-TiO_2 1 µm and 200 nm scale bar (a & b) and TiO_2 1 µm and 200 nm scale bar (c & d).

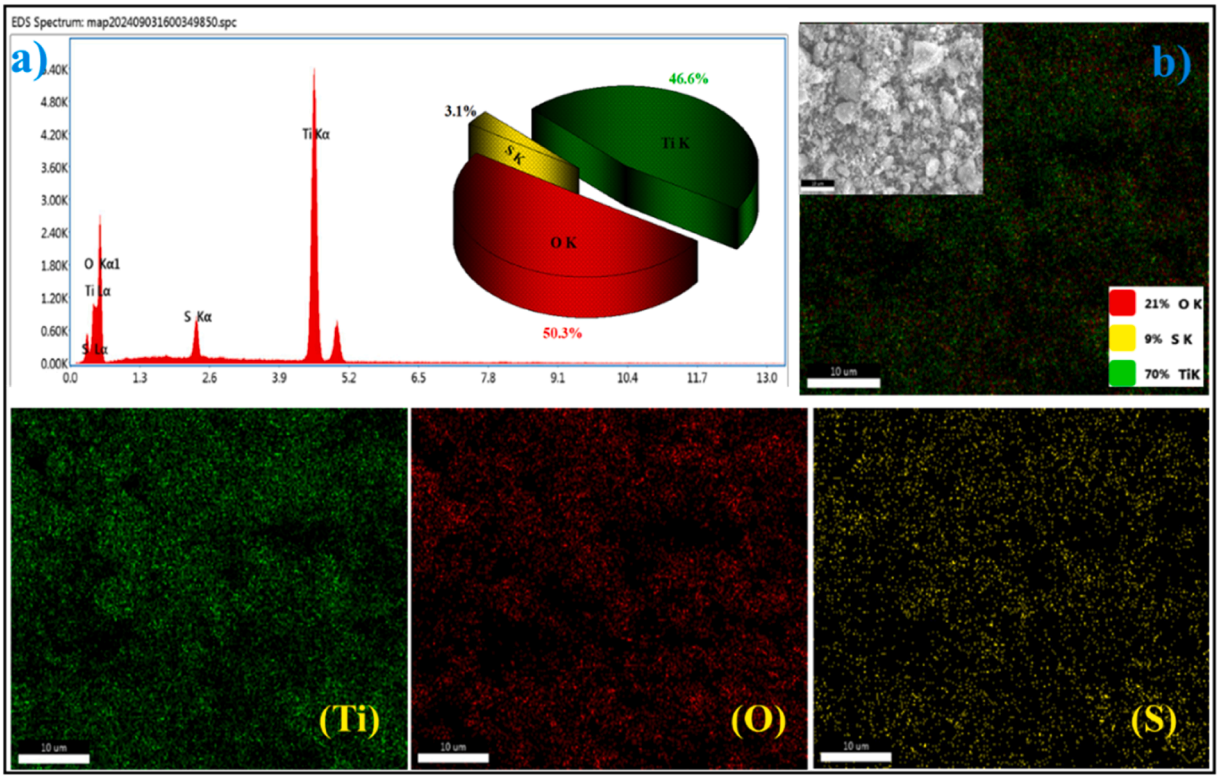

Fig. 3.. Elemental analysis (a), and Colour mapping (b) of SO_4^{2-}-TiO_2.

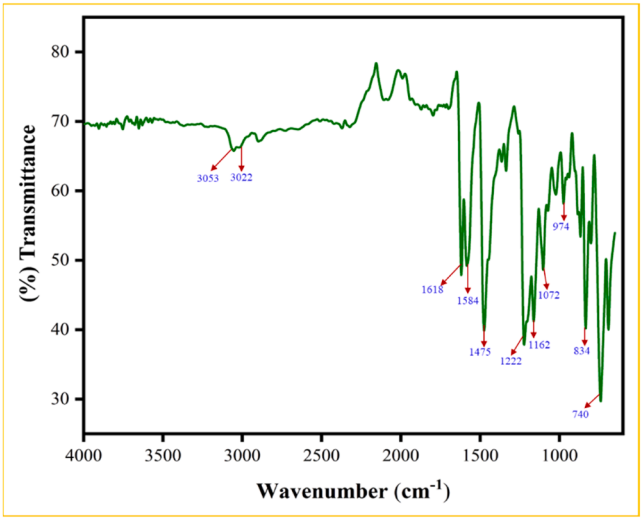

Fig. 4. FT-IR spectrum of synthesized SB 3a.

Hugo Schiff, are structurally defined by the generic formula R-HC═*N*-R', where R and R' might be alkyl, aryl, cycloalkyl, or heterocyclic units. The defining feature of SB is the azomethine (>CH═*N*<) functional moiety, which results from switching the carbonyl group in aldehydes or ketones [14–17]. SBs are especially noteworthy for their ability to coordinate with various metal ions via the nitrogen atom's lone pair electrons, resulting in stable metal complexes. Typically synthesized in the presence of acid or base catalysts or by applying heat, SBs are often crystalline solids with low basicity. However, some SBs can react with strong acids to produce insoluble salts, further expanding their versatility in chemical applications [18–20]. SBs and their derivatives have become intensively investigated owing to their numerous applications in medicinal chemistry, pharmacology, and biological sciences. They exhibit significant potential in disease treatment, functioning as therapeutic agents in various medical applications such as antibacterial, antifungal, analgesic, antitumor, anti-inflammatory, antimalarial, antiviral, antioxidant, and free radical scavenging activities. Additionally, they operate as biological regulators, facilitating metabolic reactions. Moreover, SBs are highly effective as chelating agents, allowing the production of transition metal complexes with a variety of structural and functional features [19]. The creation and manufacturing of multidentate phenoxy SB ligands and metal complexes have received attention due to their catalytic activity and potential as biological models. These ligand's electrical and structural attributes significantly impact their catalytic efficiency, and phenoxy-imine SBs derivatives are of particular interest for their unique features and wide-ranging applications [21–25]. Using Becke's three-parameter hybrid functional (B3LYP) and Density Functional Theory (DFT), quantum chemical methods provide powerful tools to analyze molecular geometry, vibrational properties, and other molecular properties [26]. In parallel, molecular dynamics (MD) simulations provide a computer framework for understanding molecule's structure and function by forecasting atomic movements over time using physical theories guiding atomic interactions. These simulations are useful for examining various biomolecular processes, including conformational changes, ligand binding, and protein folding, as they provide femtosecond temporal resolution into atomic locations [27,28].

In this study, prepared sulfated titanium dioxide (SO_4^{2-}-TiO_2) is presented as a green and sustainable alternative to conventional catalysts. Its ability to perform in mild temperatures demonstrates its potential for environmentally friendly applications. Building on our ongoing research in SO_4^{2-}-TiO_2, we devised a simple and fast approach for synthesizing new phenoxy SBs (**3a–3g**) (Scheme 1) and investigated their catalytic activity as a reusable solid acid catalyst. This technology follows green chemistry principles, offering benefits such as solvent-free conditions, low energy consumption, reusability, cost-effectiveness, and high product yields without extra purification when compared to previously described methods [19,21]. The synthesized compounds were extensively studied utilizing spectroscopic techniques (IR, NMR, single crystal XRD) and DFT calculations. Schiff's bases are renowned for their diverse pharmacological activities, including antimicrobial, analgesic, anti-inflammatory, antifungal, antiviral, and antioxidant characteristics, and have received significant interest. Based on this background, the phenoxy SBs derivatives (**3a–3g**) were synthesized and assessed for biological potential. To better understand their biological efficacy, the compounds were subjected *in-silico* ADME predictions and molecular docking to evaluate binding interactions, and molecular dynamics simulations to assess binding site ability. This combined approach highlights the possibility of using SO_4^{2-}-TiO_2-catalyzed phenoxy SBs for intriguing future applications.

2. Experimental

2.1. Material and methods

Information on the materials and characterization techniques employed in this study are detailed in the supporting materials S1. All of

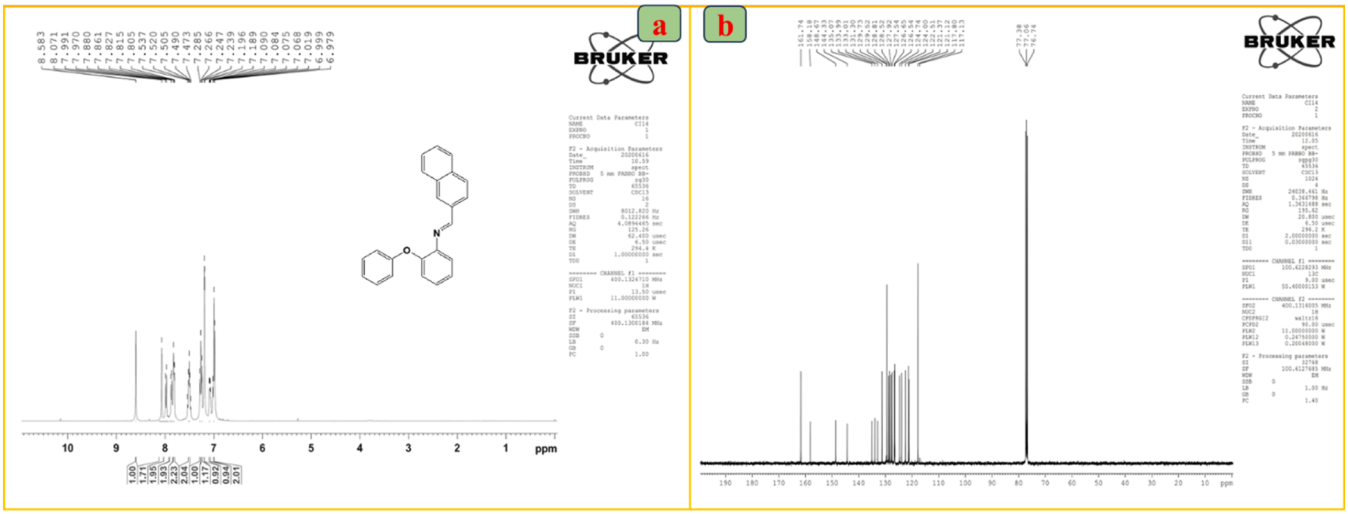

Fig. 5. ^{1}H NMR (a) ^{13}C NMR (b) spectrum of synthesized SB 3a.

Table 1
Structure refinement and crystallographic information for SB's **3d** and **3g**.

	3d		3g	
Empirical formula	$C_{19}H_{14}N_2O_3$		$C_{22}H_{21}NO_4$	
Formula weight	318.33 g/mol		363.40 g/mol	
Temperature	273(2) K		273(2) K	
Wavelength	0.71073 Å		0.71073 Å	
Crystal system	Monoclinic		Orthorhombic	
Space group	C -1_c		P 2_1	
Unit cell dimensions	a = 6.0612 (9)Å	α = 90°	a = 7.4338 (9)Å	α = 90°
	b = 38.306 (8)Å	β = 106.906°	b = 7.8234 (8)Å	β = 90°
	c = 7.1220 (14)Å	γ = 90°	c = 32.554 (4)Å	γ = 90°
Volume	1582.1(4) Å^3		2050.7(4) Å^3	
Z	4		4	
Density (calculated)	1.336 g/cm^3		1.275 g/cm^3	
Absorption coefficient	0.094 mm^{-1}		0.088 mm^{-1}	
F(000)	660		768	
Crystal size	0.250 × 0.290 × 0.360 mm^3		0.220 × 0.280 × 0.350 mm^3	
Theta range for data collection	2.13 to 30.15°		2.81 to 30.17°	
Index ranges	$-8 \le h \le 7$, $-54 \le k \le 53$, $-10 \le l \le 9$		$-10 \le h \le 10$, $-10 \le k \le 10$, $-46 \le l \le 38$	
Reflections collected	13,806		17,873	
Independent reflections	3790 [R(int) = 0.0413]		5531 [R(int) = 0.0502]	
Coverage of independent reflections	98.5 %		98.7 %	
Absorption correction	Multi-scan		Multi-scan	
Max. and min. transmission	0.7460 and 0.5657		0.9810 and 0.9710	
Refinement method	Full-matrix least-squares on F^2		Full-matrix least-squares on F^2	
Data / restraints / parameters	3790 / 2 / 217		5531 / 0 / 247	
Goodness-of-fit on F^2	1.044		1.038	
Final R indices [I > 2sigma (I)]	R1 = 0.0678, wR2 = 0.1990		R1 = 0.0479, wR2 = 0.1035	
R indices (all data)	R1 = 0.0864, wR2 = 0.2248		R1 = 0.0762, wR2 = 0.1200	
Largest diff. peak and hole	0.350 and −0.202 e.Å^{-3}		0.152 and −0.136 e. Å^{-3}	
CCDC	**2361,892**		**2362,121**	

the experimental solutions were prepared using double-distilled water.

2.2. Catalyst (SO_4^{2-}-TiO_2) preparation

To prepare the SO_4^{2-} functionalized catalyst, the sol–gel method was employed by TTIP (titanium tetraisopropoxide) as its precursor. Initially, 12.5 mL of TTIP was mixed in 100 mL of 2-propanol under constant stirring. Subsequently, 3.2 mL of 1 M sulphuric acid was introduced dropwise to the solution with vigorous stirring to ensure uniform mixing. This consequent colloidal suspension was swirled continuously for 4 h to encourage gel formation. The gel was filtered, thoroughly washed, and dried at 100 °C for 12 h. To ensure that sulfate ions were incorporated into the gel, a $BaCl_2$ test was performed on the filtrate, which produced no precipitation. This indicated that entire sulfate ions were successfully transferred onto the gel matrix. Furthermore, the dried sample was calcined at 400 °C for 1 hour in a muffle furnace [29].

2.3. General synthesis of SBs (3a-3g)

This SBs were prepared by microwave-assisted condensation of 2-phenoxyaniline (1 mmol) with aromatic aldehydes (1 mmol) in the presence of SO_4^{2-}-TiO_2 catalyst (80 mg). The reaction mixture was subjected to a microwave irradiation at 450 W for 4 min, as depicted Scheme 1. The product **3a** was isolated from dichloromethane extract by evaporation. TLC was employed to keep track of the reaction progress. The catalyst was recovered by filtration and washing with cold ethanol. The brown recrystallized solids was obtained from crude product.

2.3.1. (E)-N-((naphthalen-2-yl)methylene)-2-phenoxybenzenamine (3a)

Yield: 96 %; M.p: 86–87 °C; MF: $C_{23}H_{17}NO$; MW: 323.39. Anal. Calcd. for CHN (%): C (85.42), H (5.30), N (4.33); Found (%): C (85.38), H (5.26), N (4.30); [IR: KBr, cm^{-1}; $3053_{\mathbf{Ar\text{-}CH}}$, $1618_{\mathbf{C=N}}$, $1475_{\mathbf{C=C}}$]; [NMR: $CDCl_3$, δ ppm: ^{1}HNMR 400 MHz: 8.58(s1H), 6.97–7.99(m 16H); ^{13}CNMR 100 MHz: 161.74, 158.18, 148.67, 135.07].

2.3.2. (E)-N-benzylidene-2-phenoxyaniline (3b)

Brown recrystallized product Yield: 90 %; M.p: 56–57 °C; MF: $C_{23}H_{17}NO$; MW: 273.33. Anal. Calcd. for CHN (%): C (83.49), H (5.53), N (5.12); Found (%): C (83.53), H (5.08), N (5.08); [IR: KBr, cm^{-1}; $3043_{\mathbf{Ar\text{-}CH}}$, $1618_{\mathbf{C=N}}$, $1476_{\mathbf{C=C}}$]; [NMR: $CDCl_3$, δ ppm: ^{1}HNMR 400 MHz: 8.96(s1H), 6.95–8.07(m 14H); ^{13}CNMR 100 MHz: 158.04, 157.05, 148.33, 143.09–117.12].

2.3.3. (E)-N-(4-methylbenzylidene)-2-phenoxyaniline (3c)

Brown recrystallized product Yield: 93 %; M.p: 78–79 °C; MF: $C_{20}H_{17}NO$; MW: 287.36. Anal. Calcd. for CHN (%): C (83.59), H (5.96), N …[IR: KBr, cm^{-1}; $3034_{\mathbf{Ar\text{-}CH}}$, $2918_{\mathbf{Ali\text{-}CH}}$, $1616_{\mathbf{C=N}}$, $1484_{\mathbf{C=C}}$]; [NMR: $CDCl_3$, δ ppm: ^{1}HNMR 400 MHz: 8.40(s1H), 6.69–7.65(m 13H), 2.37 (s 3H); ^{13}CNMR 100 MHz: 161.77, 158.18, 148.52, 141.90–116.50, 21.62].

2.3.4. (E)-N-(2-nitrobenzylidene)-2-phenoxyaniline (3d)

The brown crystal exists as a monoclinic system. Yield: 90 %; M.p: 62–63 °C; MF: $C_{19}H_{14}N_2O_3$; MW: 318.33. Anal. Calcd. for CHN (%): C (71.69), H (4.43), N (8.80); Found (%): C (71.66), H (4.39), N (8.75); [IR: KBr, cm^{-1}; $3064_{\mathbf{Ar\text{-}CH}}$, $1622_{\mathbf{C=N}}$, $1510_{\mathbf{C=C}}$]; [NMR: $CDCl_3$, δ ppm: ^{1}HNMR 400 MHz: 8.93(s1H), 8.02–6.95(m 13H); ^{13}CNMR 100 MHz: 158.06, 157.57, 149.02, 143.06–116.50].

2.3.5. (E)-4-(((2-phenoxyphenyl)imino)methyl)phenol (3e)

Recrystallized brown solid Yield: 94 %; M.p: 56–57 °C; MF: $C_{19}H_{15}NO_2$; MW: 289.33. Anal. Calcd. for CHN (%): C (78.87), H (5.23), N (4.84); Found (%): C (78.91), H (5.19), N (4.79); [IR: KBr, cm^{-1}; $3045_{\mathbf{Ar\text{-}CH}}$, $1617_{\mathbf{C=N}}$, $1481_{\mathbf{C=C}}$]; [NMR: $CDCl_3$, δ ppm: ^{1}HNMR 400 MHz: 8.46(s1H), 7.31–6.69(m 13H); ^{13}CNMR 100 MHz: 159.27, 158.12, 148.52, 143.33–117.80].

2.3.6. (E)-N-(3,4-dimethoxybenzylidene)-2-phenoxyaniline (3f)

Recrystallized brown solid Yield: 95 %; M.p: 96–97 °C; MF: $C_{21}H_{19}NO_3$; MW: 333.38. Anal. Calcd. for CHN (%): C (75.66), H (5.74), N (4.20); Found (%): C (75.61), H (5.71), N (4.25); [IR: KBr, cm^{-1}; $3036_{\mathbf{Ar\text{-}CH}}$, $2935_{\mathbf{Ali\text{-}CH}}$, $1617_{\mathbf{C=N}}$, $1481_{\mathbf{C=C}}$]; [NMR: $CDCl_3$, δ ppm: ^{1}HNMR 400 MHz: 8.43(s1H), 7.32–6.71(m 12H), 3.80 (s 6H); ^{13}CNMR 100 MHz: 158.63, 158.20, 148.02, 138.79–117.11, 55.96].

2.3.7. (E)-2-phenoxy-N-(3,4,5-trimethoxybenzylidene)aniline (3g)

The brown crystal exists in an orthorhombic system. Yield: 99 %; M.p: 108–109 °C; MF: $C_{22}H_{21}NO_4$; MW: 363.41. Anal. Calcd. for CHN (%): C (72.71), H (5.82), N (3.85); Found (%): C (72.75), H (5.78), N (3.82); [IR: KBr, cm^{-1}; $3068_{\mathbf{Ar\text{-}CH}}$, $2839_{\mathbf{Ali\text{-}CH}}$, $1620_{\mathbf{C=N}}$, $1483_{\mathbf{C=C}}$]; [NMR: $CDCl_3$, δ ppm: ^{1}HNMR 400 MHz: 8.34(s1H), 7.26–7.99(m 11H), 3.87 (s 9H); ^{13}CNMR 100 MHz: 160.84, 153.37, 148.46, 140.98–117.56, 56.22].

2.4. Computational studies

All computations for compounds **3a-3g** were conducted by the GAUSSIAN 09 W software [30], employing DFT (Density Functional Theory) with the B3LYP method and a 6–311 G (d,p) basis set. GAUSSVIEW 5.0 [31] was used for the molecular visualization.

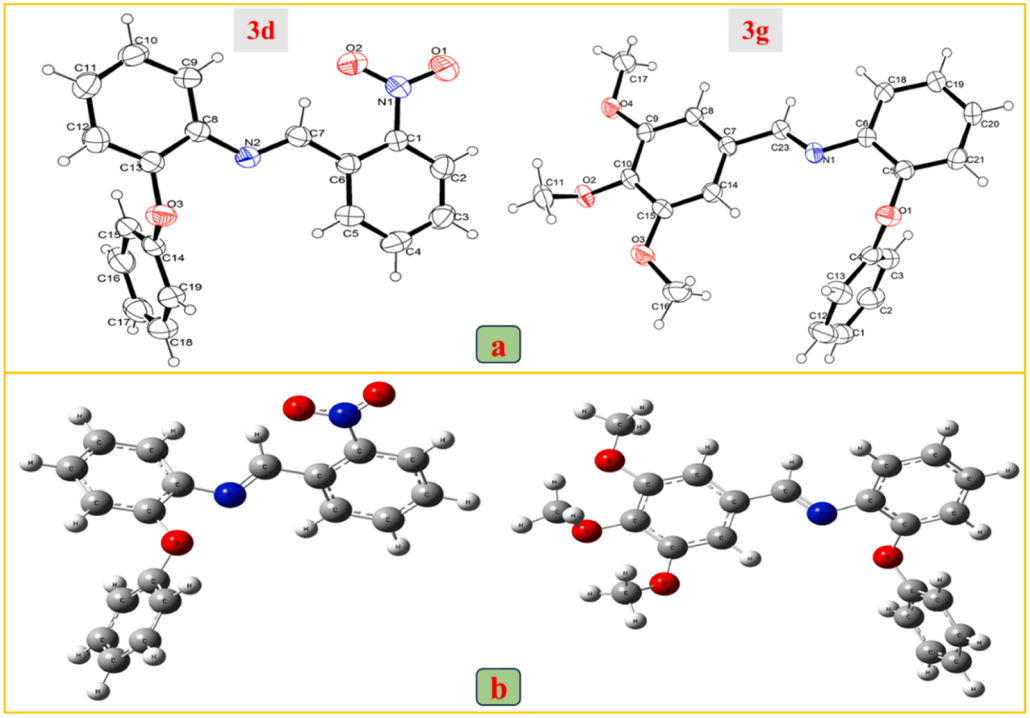

Fig. 6. Experimental ORTEP (a) Optimized structure (b) of synthesized SBs 3d and 3g.

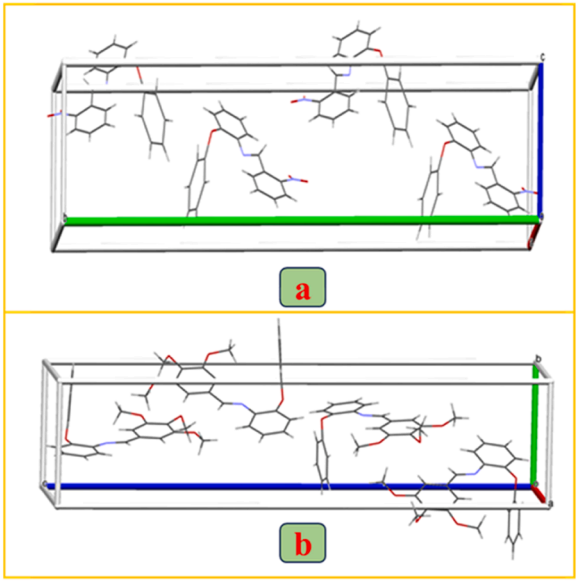

Fig. 7. Packing diagram of synthesized SBs 3d (a) and 3g (b).

Molecular docking studies were carried out using AutoDock 4.0, which provides various stochastic search methods [32]. The LGA (Lamarckian Genetic Algorithm) was chosen for this research. The 2D images were generated using the PDBSum online tool, while the 3D images were obtained from Discovery Studio. Drug-likeness properties were predicted using the SwissADME tool [33].

2.5. Antimicrobial studies

The antibacterial activity of synthesized compounds (**3a-g**) were evaluated using the disc diffusion method against human pathogenic strains, including Gram-positive (*Bacillus subtilis* and *Staphylococcus aureus*) and Gram-negative strains (*Proteus mirabilis, Salmonella paratyphi A*, and *Pseudomonas aeruginosa*), with Amoxcilin as standard drug. Following the Bauer-Kirby technique [34], the agar medium was prepared, and inocula were standardized. The compounds dissolved in chloroform and then diluted to concentrations of 20, 30, 40, and 50 μg/mL, and they were loaded onto agar wells to assess their zones of inhibition. Similarly, the antifungal activity of these compounds was tested against *Penicillium chyrsogenum, Aspergillus flavus*, and *Candida albicans* using the same Kirby-Bauer disc diffusion method, with Ampotericin-B as standard drug.

3. Results and discussions

3.1. Catalyst characterization

The FT-IR spectrum of the nano SO_4^{2-}-TiO_2 catalyst, shown in Fig. 1a, provides structural information. The IR peaks of sulfate species on the catalyst surface are mostly situated between the region of 700–1500 cm^{-1}. The hydroxyl group accounts for the large adsorption band at 3557 cm^{-1}. Sulfate ions adsorbed on the catalyst surface exhibit four peaks at 1230, 1049, 1137, and 970 cm^{-1}, indicating stretching vibrations. The bands at 1049 and 1137 cm^{-1} align with previously reported frequencies of SO_4^{2-}, indicating a strong interaction between sulfate species and the TiO_2 surface. Additionally, the peak at 1620 cm^{-1} attributed to the H—O-H bending of physically adsorbed water [35].

Fig. 1b depicts the XRD pattern of SO_4^{2-}-TiO_2. The prepared SO_4^{2-}-TiO_2 diffraction peaks exhibit similar 2θ values to those of TiO_2, but with considerable peak intensities. TiO_2-SO_4^{2-} has large fullwidth at half-maximum (FWHM) values than pure TiO_2, indicating smaller particles. The characteristic (101) plane is shown by the most conspicuous diffraction peak at 25.5°. The peaks $2\theta = 25.5°$, 47.7°, and 54.4° correspond to the TiO_2 anatase phase. The peaks at $2\theta = 27.39°$, and 35.95° belong to the (110) and (101) planes of the rutile phase of TiO_2. The crystalline size of TiO_2-SO_4^{2-} was found using Eq. (1) (Debye–-Scherrer equation) [36,37].

Table 2
Computed global metrics for SB's 3a-3g.

Schiff's base No.	Total Energy (a. u)	FMO Orbital's (eV)	Energy Gap(Δ) (eV)	Chemical potential (μ)	Electronegativity (χ)	Hardness (η)	Softness (S)	Electrophilicity (ω)
3a	−1016.6847	HOMO = −5.6841 LUMO = −1.6487	4.0354	3.6664	−3.6664	2.0177	0.2478	3.3312
3b	−863.0363	HOMO = −5.6724 LUMO = −1.5398	4.1325	3.6061	−3.6061	2.0662	0.2419	3.1468
3c	−902.3575	HOMO = −5.6330 LUMO = −1.4653	4.1677	3.5491	−3.5491	2.0838	0.2399	3.0224
3d	−1067.5202	HOMO = −5.7799 LUMO = −2.2297	3.5502	4.0048	−4.0048	1.7751	0.2816	4.5176
3e	−938.2580	HOMO = −5.5756 LUMO = −1.3649	4.2107	3.4702	−3.4702	2.1053	0.2374	2.8600
3f	−1092.6776	HOMO = −5.6226 LUMO = −1.4816	4.1410	3.5521	−3.5521	2.0705	02,414	3.0469
3g	−1206.5956	HOMO = −5.5092 LUMO = −1.3915	4.1177	2.0588	−2.0588	2.0588	0.2428	2.8911

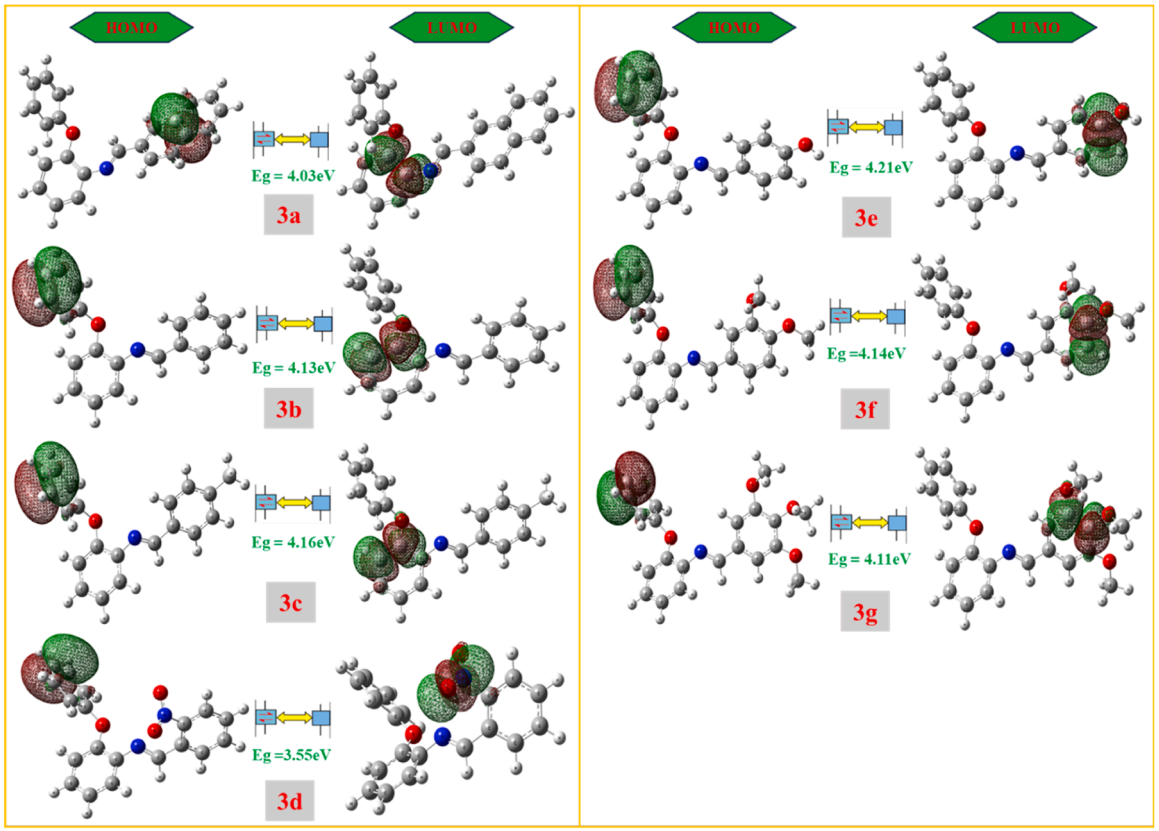

Fig. 8. LUMOs and HOMOs plots of synthesized SBs 3a-3g.

$$D = \frac{K\lambda}{\beta \cos\theta} \quad (1)$$

where D represents the crystal size of the catalyst, K is a dimensionless constant, λ denotes the wavelength of the X-ray, β is the full width at half maximum (FWHM) of the diffraction peak, and θ is the diffraction angle. The maximum intense peak at $2\theta = 25.21^{\circ}$ was utilized to determine of FWHM and the crystalline size of SO_4^{2-}-TiO_2 was calculated to be 11.52 nm.

The texture and shape of a catalyst serve as crucial characteristics that can have a considerable impact on catalytic activity. Fig. 2a–d shows SEM images of SO_4^{2-}-TiO_2 and TiO_2. The SEM images of SO_4^{2-}-TiO_2 show flake-like particle shape. Modifying with $SO4^{2-}$ ions reduces particle aggregation relative to pure TiO_2 (Fig. 2c and d). Fig. 3b shows the EDS analysis of SO_4^{2-}-TiO_2, revealing that the sulfur content in a specific region of the SO_4^{2-}-TiO_2 sample is 3.1 % by weight, as shown in Fig. 3a.

3.2. FT-IR analysis of synthesized SB's (3a-3g)

The vibrational spectra of compound **3a** are shown in Fig. 4, the main functional groups in the molecule are the aromatic hydrogens (Ar-H), the azomethine group (CH═*N*), the aromatic *C* = *C* bonds, and the oxygen atom between phenyl rings. Absorption bands in the range of 3022 - 3053 cm^{-1} are assigned to aromatic C—H stretches, while a sharp and distinctive band at 1618 cm^{-1} is attributed to *C* = *N* stretching vibration. The biphenyl ether C—O-C vibrational frequency of the imine was observed at 1222 cm^{-1}. Similarly, all characteristic infrared frequencies of remaining compounds **3b-3g** were assigned. All compounds show medium or strong absorption bands at 1616–1622 cm^{-1} indicating *C* = *N*

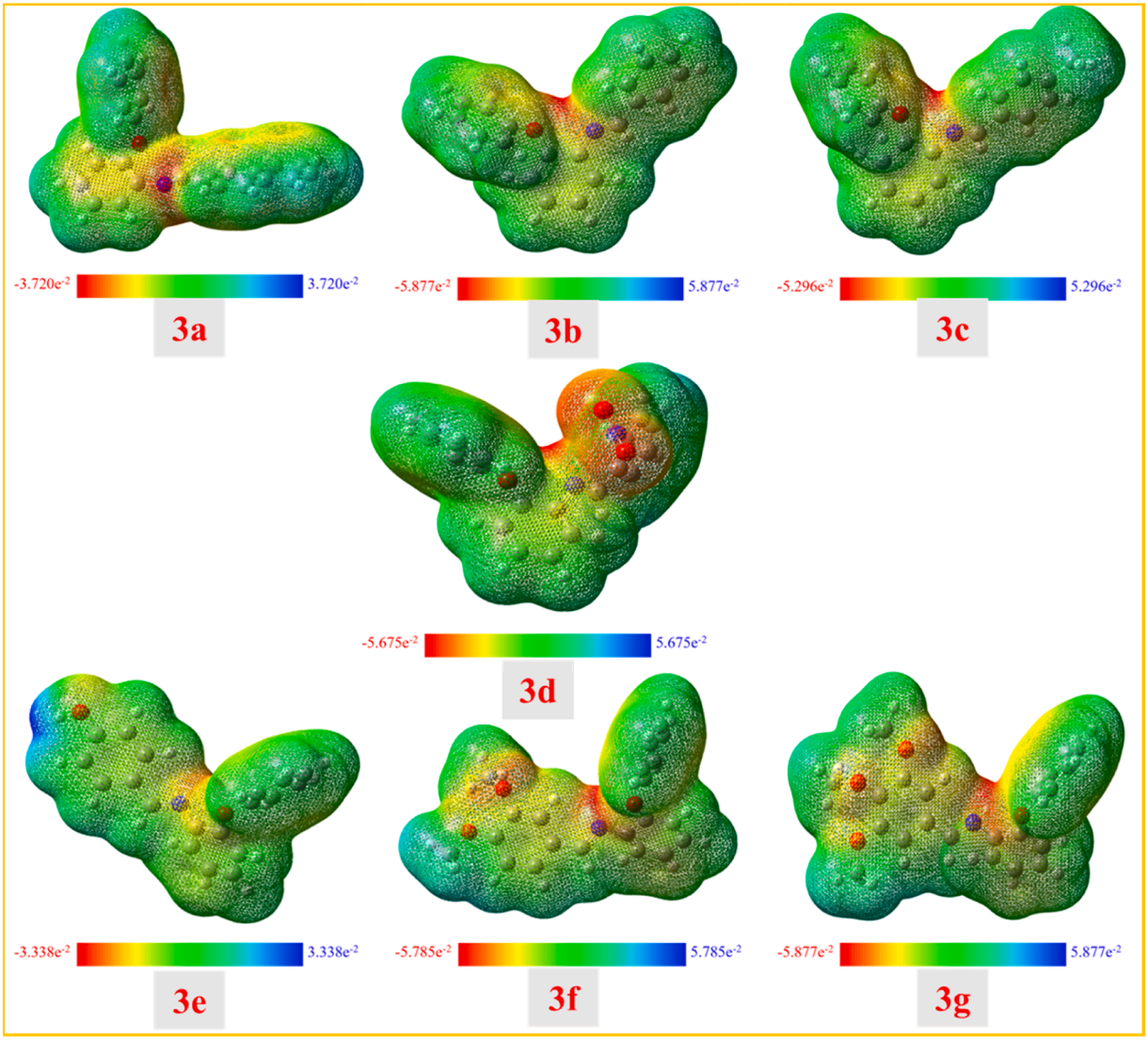

Fig. 9. MEP platform of synthesized SBs 3a-3g.

vibration [38]. The methoxy stretching vibration of compounds **3f** and **3g** was observed in the frequency range of 1156 and 1126 cm^{-1}. The assigned FT-IR spectral data of all synthesized compounds **3b-3g** are given in Table S1 and are shown in Figs. S1–S6.

3.3. NMR (^{1}H&^{13}C) analysis of SB's (3a-3g)

In this series of SBs, Fig. 5a depicts the ^{1}H NMR spectrum of **3a**. The compound 3a chemical shift (δ, ppm), observed downfield at 8.583 as a sharp single peak was represented to the imine (HC═*N*-) proton. The crowded multiplet peaks obtained in the region of 6.979 – 7.991 ppm are assigned to the aromatic protons. Similarly, the ^{1}H NMR chemical shifts (δ, ppm), the values of SBs **3b-3g** of this series are assigned and recorded in Table S2. The proton of azomethine group (HC═*N*-) shifts of all compounds and ranging from 8.344 to 8.966 ppm. Methyl and methoxy protons of the **3c, 3f** and **3g** provide an up-field signal as a singlet at 2.37, 3.94 and 3.87 ppm [39].

The compound **3a** ^{13}C NMR spectrum (Fig. 5b) shows the imine carbon (HC═*N*-) signal at 161.74 ppm, with aromatic carbon signals observed between 117.13 and 135.07 ppm. The azomethine carbon shifts for compounds **3a-3g** fall within the range of 158.04 and 161.77 ppm. The up-field signal at 21.62, 55.96, and 56.22 ppm are ascribed to the ^{13}C chemical shifts of the methyl and methoxy carbons in compounds **3c, 3f** and **3g** respectively [39]. The assigned NMR shifts of all synthesized compounds **3b-3g** are provided in Table S2 and are shown in Figs. S7-S18.

3.4. X-ray-crystal structure descriptions of SB's 3d and 3g

The single crystal X-ray investigations affirmed that compound **3d** forms crystal in the monoclinic structure and has a space of group C-1c and compound **3g** crystallized as an orthorhombic structure and has a space group of P-2_1. The measured cell parameters are 6.061(9) 38.306 (8) and 7.120(4) Å for a, b, and c; β = 106.90° and α = γ = 90° for compound 3d and 7.433(9), 7.823(8), and 32.554(13) Å for a, b, and c; α = β = γ = 90° for compound **3g** The skeleton of compounds adopts as *E*-configuration with the four molecules in the units. The crystallographic data and refinement parameters are summarized in Table 1. Fig . 6(a and b) and 7 show the ORTEP structure, the optimized molecular structure with atom numbering, and the compound packing diagram. The dihedral angle, which consist of azomethine group for compounds **3d** and **3g** is (C6-C7-N2-C8), (C6-N1-C23-C7) is observed 178.9(3) and 176.9(2), indicating non-planar configuration both molecules.

DFT calculations using the B3LYP functional and 6–31G(d,p) basis set were performed to optimize the molecular structures. The calculated parameters of the compounds were compared with experimental X-ray

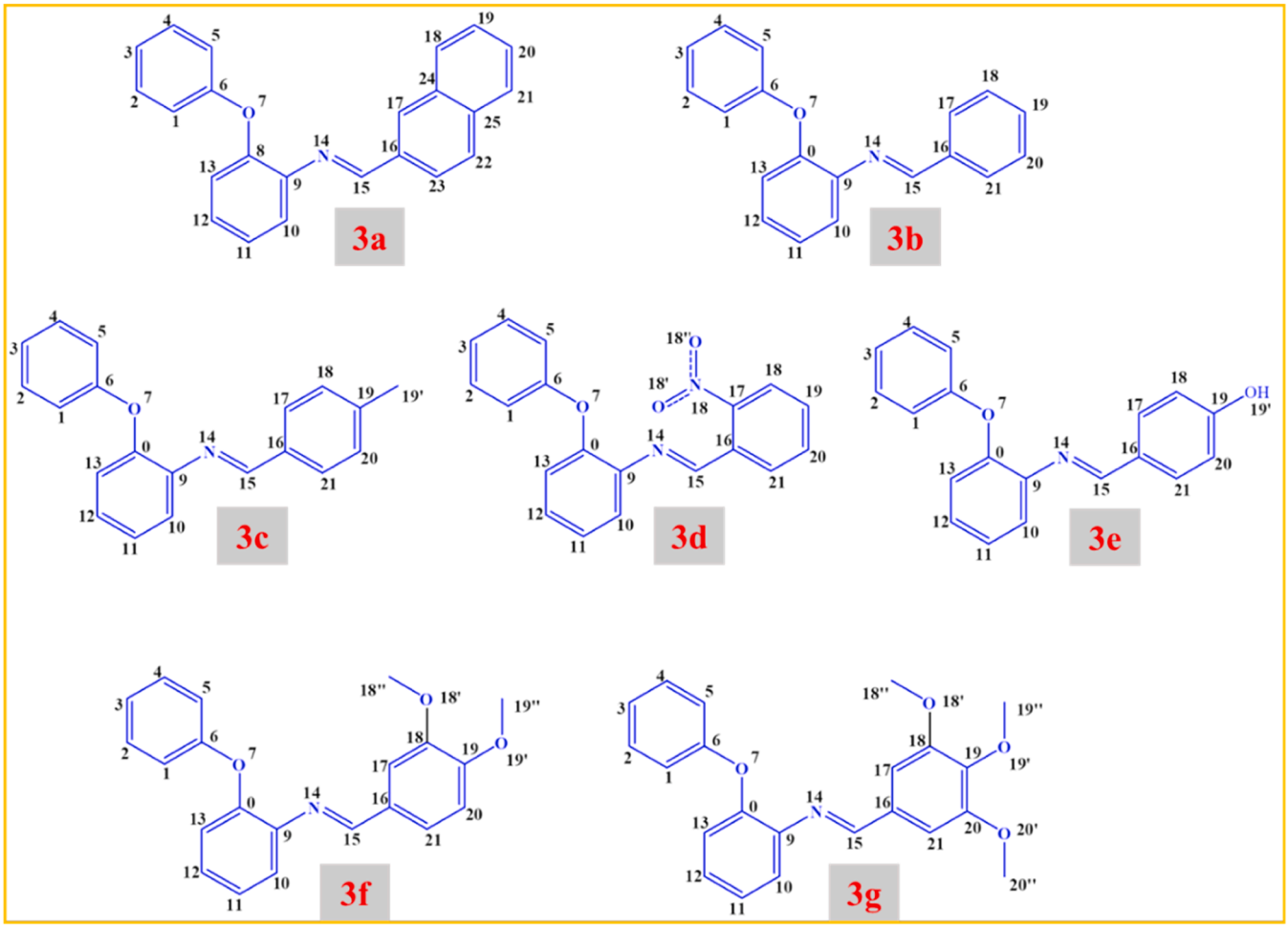

Fig. 10. Mulliken Numbering Pattern of SBs 3a-3g.

data and are displayed in Tables S3 and S4. In the phenyl ring all the C—C bond lengths of compounds **3d** and **3g** were observed in the range of 1.370–1.404 Å and 1.365–1.396 Å. Also, the azomethine bond length of compound **3d** is 1.251 Å (calculated: 1.27 Å) for N(2)-C(7) and compound **3g** is 1.254 Å (calculated:1.28 Å) for N(1)-C(23) exhibiting the π-conjugated double bond character. The bond angle of C(7)-N(2)-C (8) was determined to be 120.9° (calculated:120.01°) for compound **3d** and the bond angle of C(23)-N(1)-C(6) was found to be 121.0° (calculated: 119.76°) [38,40] for compound **3g** and these values are presented in Tables S3 and S4. The optimized molecular structures of the remaining compounds are shown in Fig. S19. All these compounds revealed *E* confirmation with the azomethine group.

3.5. Electronic structure of SB's (3a-3g)

Frontier molecular examination is a highly effective way for investigating a molecule's potential for charge transfer, chemical solidity, absorption spectra, and optoelectronic characteristics for the synthesized SBs. FMOs involve two molecular orbitals with varying energy gaps: the electron accepting (LOMO) and the electron donating (HOMO). The chemical properties, such as softness, hardness, reactivity, and stability, of the substance under investigation are clarified by the quantum orbital energy gap ($E_{LUMO}-E_{HOMO}$). Large HUMO−LUMO band gaps are associated with harder, less reactive, and dynamically stable molecules. A compound's hyperpolarizability factor is increased by a smaller energy gap because it allows for better internal charge transfer [41]. As a result, the molecule becomes softer, more reactive, and thus high polarizable when the energy difference between FMOs is smaller, acting as the leading NLO candidate.

Table 2 shows the calculated HOMO and LUMO energies for compounds **3a-3g** The HOMOs span from −5.77 to −5.50 eV, while the LUMOs are found between −2.22 and −1.36 eV, according to the FMOs analysis. The internal charge transfer within the molecule can be found using FMO surface diagrams. Compounds **3a-3g** exhibit electronic density around the HOMO orbital due to the free phenyl ring in the phenoxy group; in contrast, compounds **3e-3g** exhibit charge density around the azomethine group attached with phenoxy phenyl ring, while compounds **3a-3c** exhibit in substituted phenyl ring (Fig. 8). While the energy differences between **3a** and **3g** are somewhat similar, **3e** has a significantly larger band gap than the compounds mentioned before. Additionally, it has gap energies (ΔE) that range from 4.21 to 3.55 eV. Out of all the compounds studied, **3d** had the lowest band gap, with a ΔE of 3.55 eV. This could be as a result of the high electron withdrawing effect nitro (NO_2) group in nitrobenzene, which could strengthen the resonance effect and intensify the intramolecular charge transfer (ICT) process [42]. According to the findings, the examined compound's gap energies (ΔE) are arranged in ascending order as follows: **3d** < **3a** < **3g** < **3b** < **3f** < **3c** < **3e**.

3.6. Global reactivity parameters (GRPs) of SB's (3a-3g)

Numerous reactivity measures, including electron affinity (EA), ionization energy (IP), electronegativity (x), softness (σ), and chemical hardness (η), were calculated using the FMO method. Ionization energy, which is associated with EHOMO, provides information regarding the extraction of an electron from a molecule [43]. The produced

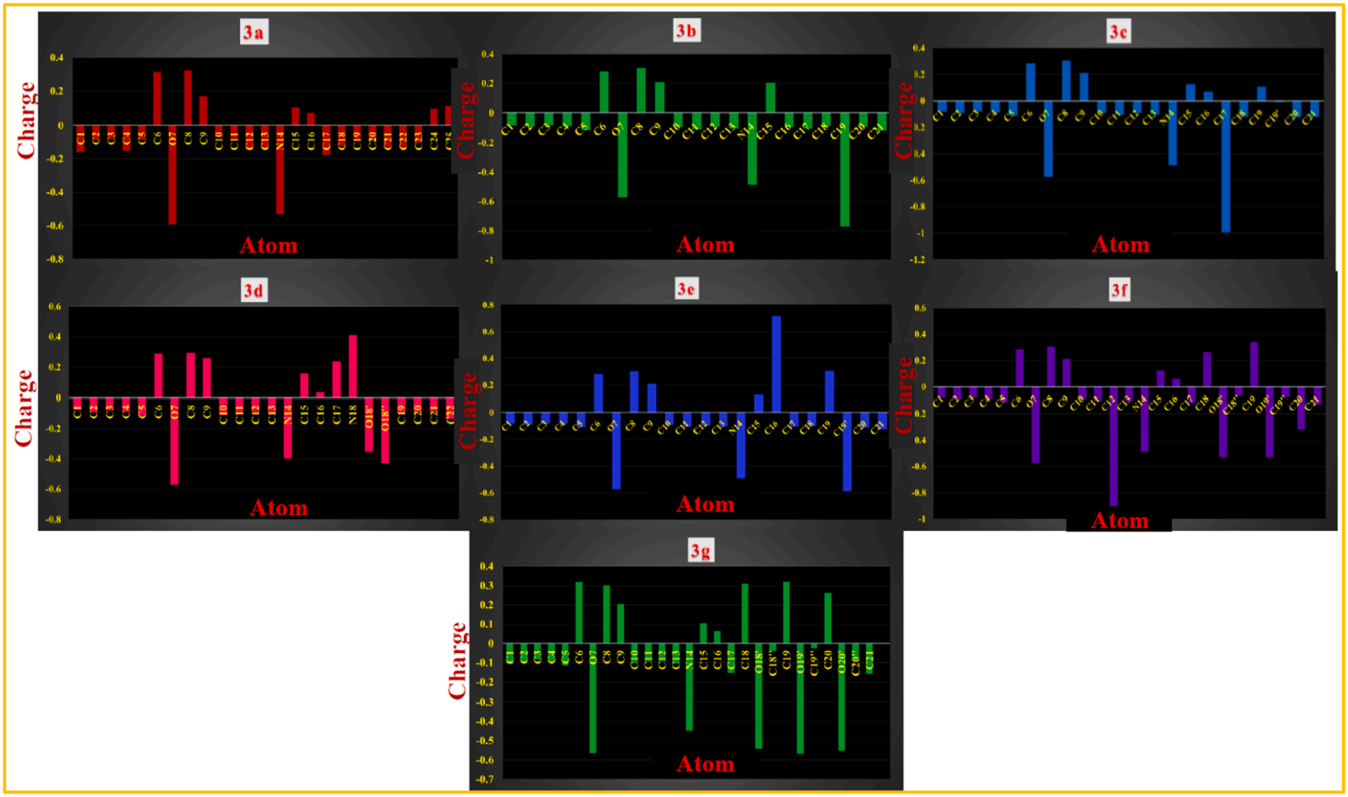

Fig. 11. Mulliken Charges of SBs 3a-3g.

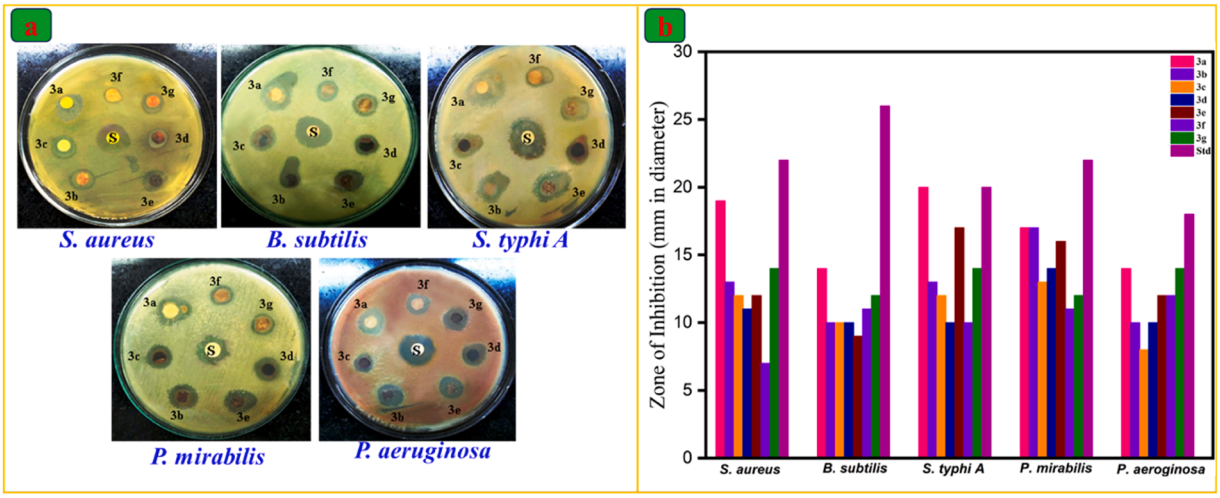

Fig. 12. Antibacterial efficiency (a) and zone of inhibition chart (b) of SBs 3a-3g.

compound's ionization energies varied from 5.50 to 5.77 eV. Compound **3d** exhibits the maximum ionization energy of 5.77 eV, while compound 3e displays the lowest ionization energy. Comparing compound **3g** to other compounds, its lower ionization energy indicates a simpler process for removing electrons.

Electron affinity (EA) is another important aspect of chemical reactivity. The EA is described as the amount of energy liberated while an electron is added to a molecule, the EA is the opposite of the IP. 1.36 to 2.22 eV were recorded as the computed electron affinity values in this investigation. Contrary to compound **3d**, which shows the maximum amount of energy release at 2.22 eV, compound **3g** demonstrated a lower electron affinity. Additionally, softness and hardness can be used to assess the molecule's polarizability. When a molecule has a lower hardness value and a higher softness value, it is more polarizable. Compound **3d** is more polarizable than the other produced compounds because of its high softness and low hardness characteristics. Table 2 provides a collection of certain FMO parameters. Considering all things, the FMO analysis gave rise to a thorough comprehension of the chemical nature of the produced compounds in addition to explaining their electrical structure and reactivity [44].

3.7. *Molecular electrostatic potential surface of SB's (3a-3g)*

Based on MEP (Molecular Electrostatic Potential) studies, the authors investigated the MEP properties of synthesized SBs **3a-3g**. The MEP surface of all synthesized SBs is shown in Fig. 9. In most cases, the

Table 3
Antibacterial efficiency of SB's **3a-3g**.

SB's No.	Zone of inhibition (mm)				
	Gram-positive			Gram-negative	
	S. aureus	*B. subtilis*	*Salmonella typhi A*	*P. mirabilis*	*P. aeruginosa*
3a	19	14	20	17	14
3b	13	10	13	17	10
3c	12	10	12	13	8
3d	11	10	10	14	10
3e	12	9	17	16	12
3f	7	11	10	11	12
3g	14	12	14	12	14
Amoxicillin	22	26	20	22	18

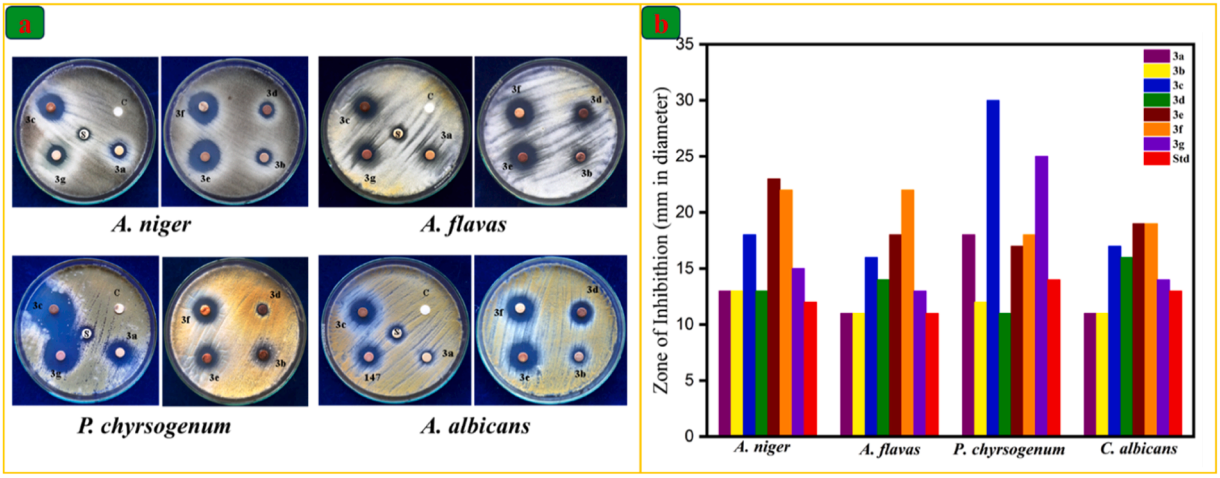

Fig. 13. Antifungal efficiency (a) and zone of inhibition chart (b) of SBs 3a-3 g.

Table 4
Antifungal efficiency of SB's **3a-3g**.

SB's No.	Zone of Inhibition (mm in diameter)			
	A. niger	*A. flavus*	*P. chyrsogenum*	*C. albicans*
3a	13	11	18	11
3b	13	11	12	11
3c	18	16	30	17
3d	13	14	11	16
3e	23	18	17	19
3f	22	22	18	19
3g	15	13	25	14
Amphotericin-B	12	11	14	13

azomethine group, nitro group oxygen (**3d**) and methoxy moiety in the imines (**3f** and **3g**) react as a electrophilic zone, marked in red colour.

Moreover, the nucleophilic zones have been shown in blue colour. As demonstrated in Fi. 9, the charge distribution differs depending on the number and position of substituent groups [42]. Molecular surfaces are developed by B3LYP level with the 6–31 G (d,p) basis set.

3.8. Mulliken charge analysis of SB's (3a-3g)

Fig. 10 depicts atom labeling using a number scheme. The Mulliken atomic charges dispersal chart for this series of SBs **3a-3g** is shown in Fig. 11 and the charges are tabulated in Table S5.

As indicated in this table, O7 and N14 atoms of compounds **3a-3g**, oxygen atoms (O18′, O18′' and O19′) of compounds **3d, 3e** and methoxy group oxygen atoms (O18′ and O19′, O20′) of compounds **3e, 3f** have most negative charge and operate as donor atoms. So, the carbon atom

Table 5
Minimum Inhibitory Concentration values of synthesized SB's **3a-3g**.

SB's No.	Minimum Inhibitory Concentration against some pathogenic microorganisms (μg/mL)								
	Bacterial Strains					Fungal Strains			
	S. aureus	*B. subtilis*	*S. typhi A*	*P. mirabilis*	*P. aeruginosa*	*A. niger*	*A. flavus*	*P. chyrsogenum*	*C. albicans*
3a	30	30	30	30	30	30	30	30	30
3b	30	30	30	30	30	30	30	30	30
3c	30	30	30	30	50	30	30	30	30
3d	30	30	40	30	40	30	30	40	30
3e	30	50	30	30	30	30	30	30	30
3f	40	30	40	40	30	30	40	30	30
3g	30	30	30	30	30	30	30	40	30
Amoxicillin	20	20	20	20	20	NA	NA	NA	NA
Amphotericin-B	NA	NA	NA	NA	NA	20	20	20	20

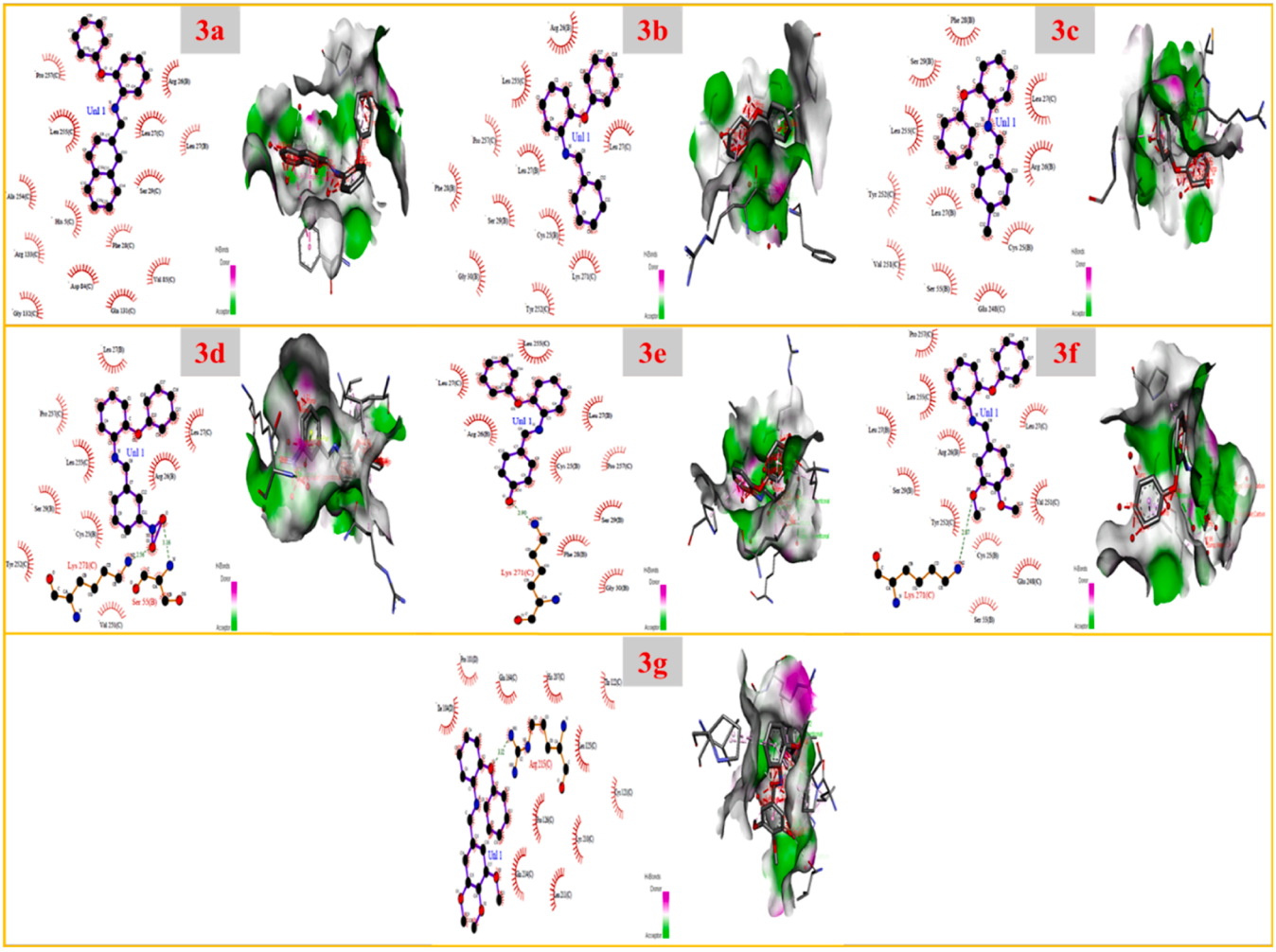

Fig. 14. Molecular docking (Protein-Ligand) interactions of 3a-3g.

Table 6
Molecular Docking properties of SB's **3a-3g** against 4Z3D.

PDB Code: 4Z3D							
Ligand	3a	3b	3c	3d	3e	3f	3g
Binding energy	−7.22	−6.43	−6.97	−7.03	−6.65	−7.15	−5.78
Ligand efficiency	−0.29	−0.31	−0.32	−0.29	−0.3	−0.29	−0.21
Inhib_Constant (μM)	5.08	19.49	7.83	7.06	13.24	5.79	57.95
Intermol_energy	−8.42	−7.62	−8.16	−8.52	−8.15	−8.93	−7.87
Vdw_hb_Desolv_energy	−8.39	−7.61	−8.13	−8.44	−7.19	−8.65	−7.8
Electrostatic energy	−0.02	−0.01	−0.03	−0.08	−0.24	−0.29	−0.07
Total_internal	−1.03	−1.1	−1.23	−1.05	−1.22	−1.11	−2.13
Torsional energy	1.19	1.19	1.19	1.49	1.49	1.79	2.09
Unbound energy	−1.03	−1.1	−1.23	−1.05	−1.22	−1.11	−2.13
Ref RMS	53.68	49.65	48.75	48.02	48.4	49.51	71.18

of azomethine moiety (C15) and the carbons C6, C8, and C15 of compounds **3a-3g,** hydroxyl proton of imine **3e** and methoxy group connected phenyl carbons [(C18, C19) and (C18, C19, and C20)] of compounds **3e** and **3f** have positive energy. They act as acceptor atoms. All the hydrogen atoms of imines **3a-3f** displayed a net positive charge [45,46].

3.9. Antimicrobial studies of SB's (3a-3g)

3.9.1. Antibacterial efficiency

In this study, the antibacterial efficiency of SBs **3a-3g** is displayed in Fig. 12 and the inhibition zone values are reported in Table 3. The compound **3a**, containing a 2-naphthyl moiety, exhibited strong antibacterial activity against *S. aureus*, while compounds **3b-3g** (bearing 1-phenyl, 4-methyl, 2-nitro, 4-hydroxy, 3,4-dimethoxy, and 3,4,5-trimethoxy substituents) demonstrated moderate activity. Poor activity was observed across all compounds against *B. subtilis*, likely due to the *+I*, *+R*, -I, and steric effects of the substituents. Compounds **3a, 3e**, and **3g** (with 2-naphthyl, 4-hydroxyphenyl, and trisubstituted phenyl groups) showed good activity against *S. paratyphi A* and *P. aeruginosa*, while others displayed moderate effectiveness.

For *P. mirabilis*, compounds **3a, 3b** and **3e** (2-naphthyl, phenyl, and

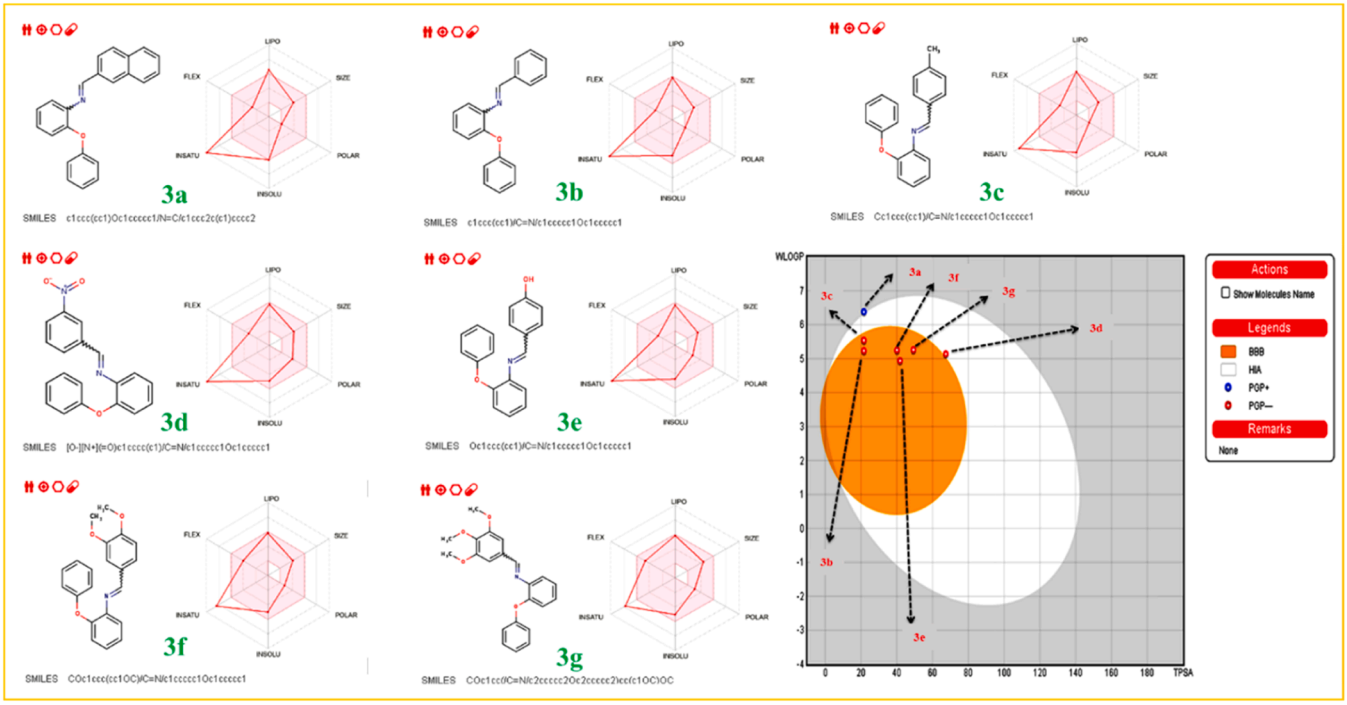

Fig. 15. Bioavailability of SBs 3a-3g.

Table 7
Impact of catalyst variations and sulfated-TiO_2 optimization on SB 3g synthesis.

Entry	Catalyst	Time (Min.)	Energy (Watts)	Yield %
1	Without Catalyst	10	450–600	No rxn
2	ZnO	10	450–600	18
3	$ZnWO_4$	10	450–600	16
4.	CuO	10	450–600	21
5	$CuFe_2O_4$	10	450–600	44
6	Prepared TiO_2	7	450–600	83
7	Sulfated-TiO_2	3–5	450–600	94
8	Sulfated-TiO_2 (60 mg)	4	450	92
9	**Sulfated-TiO_2 (80mg)**	**4**	**450**	**99**
10	Sulfated-TiO_2 (100 mg)	4	450	98
11	Sulfated-TiO_2 (120 mg)	4	450	97.5
12	Conventional method	480	Reflux	76

4-hydroxyphenyl groups) had better activity, with moderate performance from other compounds due to the effects of methoxy, nitro, and methyl groups. Most of the compounds exhibited moderate to strong activity, with MIC (Minimum Inhibition Concentration) values at 30 μg/mL in chloroform, as shown in Table 5.

3.9.2. *Antifungal efficiency*

The antifungal activities of synthesized SBs **3a-3g** were displayed in Fig. 13 and Table 4, show that all compounds exhibited excellent efficiency against *A.flavus* and *A. niger*. The **SBs 3a, 3c, 3e, 3f** and **3g** (with 2-naphthyl, 4-methylphenyl, 4-hydroxyphenyl, 3,4-dimethoxyphenyl, and 3,4,5-trimethoxyphenyl groups) displayed excellent activity against *P. chrysogenum*, while compounds **3b** and **3d** showed good activity.

The *+I*, *+R*, -I, and steric effects of phenoxy, phenyl methyl, methoxy, hydroxy, and nitro groups played a crucial role in enhancing antifungal potency. Additionally, compounds **3c-3g** exhibited better antifungal activity against *C. albicans*, with compounds **3a** and **3b** showing good activity, driven by similar substituent effects. Most of the compounds revealed good activity, with MIC values at 30 μg/mL in chloroform, as shown in Table 5.

3.10. *Molecular docking studies of SB's (3a-3g)*

The docking studies were executed by the Autodock software package. The protein 4Z3D (Human Carbonyl Reductase) was downloaded from the RCSB-PDB database, and pre-processing steps such as water removal and the addition of polar hydrogen atoms were conducted using Discovery Studio Visualizer [47,48]. The synthesized SBs compounds **3a-3g** were docked with the 4Z3D protein and displayed in Fig. 14. Compound **3a**, with a 2-naphthyl moiety, exhibited the highest binding affinity, the compound **3g** with a trimethoxyphenyl substitution showed the lowest. The binding affinity values are listed in Table 6, with the order of affinity being **3a** > **3f** > **3d** > **3c** > **3e** > **3b** > **3g** The compounds **3d** (Ser 55(B) and Lys 217(C) with the bond length of 3.16 Å and 2.56 Å), **3e** (Lys 271(C) with the bond length of 2.90 Å), **3f** (Lys 271(C) with the bond length of 2.87 Å) and **3g** (Arg 215(C) with the bond length of 3.32 Å) show hydrogen bonding [32].

3.11. *In silico prediction of drug-likeness and ADMET analysis of SB's (3a-3g)*

In drug construction, significant biological activity in synthesized compounds is required but it is inadequate for them to be classified as drugs. Some molecules are left out owing to poor bioavailability and toxicity. Predicting pharmacokinetic and toxicity profiles for highly active molecules is a crucial step. In this study, the drug-like properties of compounds **3a-3g** were assessed using the SwissADME online tool [49]. According to the data in Table S6, the molecular weights of the compounds are under 500 g/mol, while the topological polar surface area (TPSA) and rotational bonds number remain below 140 $Å^2$ and 10, accordingly. This suggests that the synthesized SBs can form flexible interactions with targets. The LogP values for these molecules are below 5, suggesting potential solubility in aqueous solutions. Furthermore, the hydrogen bond acceptors and donor numbers are below 10 and 5, respectively. As a result, the synthesized SB compounds follow to Lipinski, Verber, Egan, and Muegge criteria, demonstrating excellent oral bioavailability properties [33].

The BOILED-Egg model, which balances polarity and lipophilicity,

shows that small molecules with higher values for gastrointestinal (GI) absorption and blood-brain barrier (BBB) permeability can be efficiently transported within body tissues. Fig. 15 presents the oral bioavailability radar and the BOILED-Egg plot for SBs **3a-3g** The high skin permeability values (Log Kp = −4.01 to −5.21 cm/s) and GI absorption, combined with BBB penetration data, indicate that these compounds **3a-3g**, may be promising therapeutic candidates [50].

3.12. Catalyst optimization for SB synthesis

When a solvent-free mixture of 3,4,5-trimethoxybenzaldehyde and 2-phenoxyaniline was microwave irradiated (450 W) for 5 min, no reaction was observed. Prolonging the irradiation caused evaporation and charring. However, adding a catalytic amount of SO_4^{2-}-TiO_2 to the mixture initiated a condensation reaction, yielding 99 % of the imine (**3g**) within 4 min (Scheme 1, Table 7, entry 9).

Comparitively, prepared TiO_2 (without sulfate) under the same conditions resulted in an 83 % yield after 7 min and some other catalysts also did not create a notable impact on that reaction. The effect of catalyst (SO_4^{2-}-TiO_2) quantity was further examined, with the yield increasing from 92 % to 99 % as the catalyst amount rose from 0.06 g to 0.08 g. Beyond 0.08 g, no significant improvement in conversion was observed. The optimal catalyst loading for the synthesis of SB **3g** [3,4,5-trimethoxybenzaldehyde and 2-phenoxyaniline (1:1 mmol)] was determined to be 0.08 g.

4. Conclusions

FT-IR and powder XRD analysis showed the successful fabrication SO_4^{2-}-TiO_2 with distinct sulfate peaks, crystalline phases, and a crystalline size of 11.52 nm. SEM imaging indicated a flake-like morphology with reduced particle aggregation, and EDS analysis confirmed sulfur incorporation, demonstrating successful surface modification of the catalysts. Sulfated titania was proved to be highly effective solid acid catalyst for the solvent-free microwave-aided synthesis of new phenoxy SBs (**3a-3g**) by combining 2-phenoxyaniline with different aromatic aldehydes. This green technology produced exceptionally high yields (90–99 %) in remarkably short reaction times (4 min).

The structural investigation of the synthesized compounds was validated through FT-IR, ^{1}H NMR, and ^{13}C NMR analyses, with compounds **3d** and **3g** showing crystalline structures, demonstrating the catalyst's efficiency and selectivity. Compared to traditional and recent approaches, our methodology provided a non-toxic, cleaner, and more sustainable alternative with simpler workup and maximal efficiency for SBs formation. Furthermore, antimicrobial assessments revealed activity against bacterial and fungal strains, with substituent groups influencing efficacy. Molecular docking studies using AutoDock highlighted strong ligand-receptor interactions at the active site of the 4Z3D protein, with compound **3a** exhibiting the most favourable binding energy. ADME analysis further supported the medicinal potential of these compounds, revealing no significant physicochemical deviations or harmful metabolic feedback, establishing them as attractive candidates for therapeutic uses.

CRediT authorship contribution statement

N. Dinesh kumar: Writing – original draft, Methodology, Investigation, Formal analysis, Conceptualization. **S. Rajmohan:** Software, Investigation. **K. Selvakumar:** Resources, Formal analysis. **D. Rajamanickam:** Formal analysis. **G. Thirunarayanan:** Writing – review & editing, Supervision, Investigation. **M. Swaminathan:** Writing – review & editing, Validation, Supervision, Investigation.

Declaration of competing interest

The authors declare that they have no known competing financial interests or personal relationships that could have appeared to influence the work reported in this paper.

Acknowledgments

The authors thank Kalasalingam Academy of Research and Education (KARE) for providing the necessary facilities to carry out this work and Department of Chemistry, Annamalai University for recording Single-Crystal XRD data.

Supplementary materials

Supplementary material associated with this article can be found, in the online version, at doi:10.1016/j.molstruc.2025.142824.

Data availability

Data will be made available on request.

References

[1] M.A.C. Sundari, A. Jha, K.R. Amperayani, V.M. Chand, Design, ultrasonic synthesis, antimicrobial activity and molecular docking studies of pyridine-2,6-dithiazole/dioxazole analogues, J. Mol. Struct. 1316 (2024) 139063, https://doi.org/10.1016/j.molstruc.2024.139063.
[2] Vishali, S. Sharma, K. Bhatrola, A. Irfan, N. Devi, K. Mishra, K. Dubey, A. Mittal, E. Mateev, V.K. Vashistha, Green Synthesis of imidazoles: the catalytic efficacy of magnetic nanoparticles, Tetrahedron (2024) 134246, https://doi.org/10.1016/j.tet.2024.134246.
[3] L. Shiri, M. Kazemi, Fe_3O_4 MNPs-DETA/benzyl-Br_3: a new magnetically reusable catalyst for the oxidative coupling of thiols, phosphorus, sulfur, Silicon Relat. Elem. 192 (2017) 1171–1176, https://doi.org/10.1080/10426507.2017.1347654.
[4] M. Marimuthu, B. Ramalingam, B. Subramanian, W. Song, S. Kaliyamoorthy, Synthesis and characterization of Ag-Au loaded SiO_2 nanocomposites and study of its catalytic applicability in Mannich reaction, Inorg. Chem. Commun. 153 (2023) 110808, https://doi.org/10.1016/j.inoche.2023.110808.
[5] A. Roucoux, J. Schulz, H. Patin, Reduced transition metal colloids: a novel family of reusable catalysts? Chem. Rev. 102 (2002) 3757–3778, https://doi.org/10.1021/cr010350j.
[6] L.K. Yeung, R.M. Crooks, Heck heterocoupling within a dendritic nanoreactor, Nano Lett. 1 (2001) 14–17, https://doi.org/10.1021/nl0001860.
[7] K.R. Gopidas, J.K. Whitesell, M.A. Fox, Synthesis, characterization, and catalytic applications of a palladium-nanoparticle-cored dendrimer, Nano Lett. 3 (2003) 1757–1760, https://doi.org/10.1021/nl0348490.
[8] V. Dixit, G. Kumar, P. Kumar, A. Soni, M. Nemiwal, Emerging strategies for synthesis of heterocyclic compounds enabled by titanium oxide nanoparticles as heterogeneous catalyst, Tetrahedron 160 (2024) 134039, https://doi.org/10.1016/j.tet.2024.134039.
[9] Y. Tian, B. Chen, S. Zhang, Y. Zhang, Acidic ionic liquid-functionalized ordered mesoporous polymers: highly efficient solid acid catalysts for water-medium organic reactions, Chem. Eng. J. 479 (2024) 147782, https://doi.org/10.1016/j.cej.2023.147782.
[10] T. Okuhara, Water-tolerant solid acid catalysts, Chem. Rev. 102 (2002) 3641–3666, https://doi.org/10.1021/cr0103569.
[11] L.J. Konwar, P. Mäki-Arvela, J.-P. Mikkola, SO_3H-containing functional carbon materials: synthesis, structure, and acid catalysis, Chem. Rev. 119 (2019) 11576–11630, https://doi.org/10.1021/acs.chemrev.9b00199.
[12] S. Singhal, S. Agarwal, S. Arora, N. Singhal, A. Kumar, Solid acids: potential catalysts for alkene–isoalkane alkylation, Catal. Sci. Technol. 7 (2017) 5810, https://doi.org/10.1039/C7CY01554B.
[13] N.D. Kumar, G. Thirunarayanan, R. Elancheran, P. Suppuraj, L. Guganathan, R. Sivasakthikumaran, S. Ramkumar, M. Swaminathan, Solid acid-catalyzed green synthesis of bis-schiff bases: spectroscopic, DFT, molecular docking, and ADMET studies, J. Mol. Struct. 1322 (2024) 140603.
[14] V. Ambike, S. Adsule, F. Ahmed, Z. Wang, Z. Afrasiabi, E. Sinn, F. Sarkar, S. Padhye, Copper conjugates of nimsulide schiff bases targeting VEGF, COX and bcl-2 in pancreatic cancer cells, J. Inorg. Biochem. 101 (2007) 1517–1524, https://doi.org/10.1016/j.jinorgbio.2007.06.028.
[15] R. Katwal, H. Kaur, B.K. Kapur, Applications of Copper-Schiff's base complexes: a review, Sci. Rev. Chem. Commun. 3 (2013) 1–15.
[16] S. Omidi, A. Kakanejadifard, A review on biological activities of Schiff base, hydrazone, and oxime derivatives of curcumin, RSC Adv. 10 (2020) 30186–30202, https://doi.org/10.1039/D0RA05720G.
[17] O. Gungor, P. Gurkan, Synthesis and spectroscopic properties of novel asymmetric Schiff bases, Spectrochim. Acta A Mol. Biomol. Spectrosc. 77 (2010) 304–311, https://doi.org/10.1016/j.saa.2010.05.027.
[18] M.T. Islam, N.A. Bitu, B.M. Chaki, M.J. Hossain, M.A. Asraf, M.F. Hossen, M. Kudrat-E-Zahan M.A. Latif, Water-soluble Schiff base ligands and metal complexes: an overview considering green solvent, RSC Adv. 14 (2024) 25256–25272, https://doi.org/10.1039/D4RA04310C.

[19] S. Şahin, 3, 4-difluoro-2-(((4-phenoxyphenyl) imino) methyl) phenol with in silico predictions: synthesis, spectral analyses, ADME studies, targets and biological activity, toxicity and adverse effects, site of metabolism, taste activity, J. Mol. Struct. 1317 (2024) 139136, https://doi.org/10.1016/j.molstruc.2024.139136.

[20] M. Manimohan, M. Rahaman, S. Pandiaraj, M. Thiruvengadam, S. Pugalmani, Exploring biological activity and In-vitro anticancer effects of a new biomaterial derived from Schiff base isolated from Homarus americanus (Lobster) shell waste, Sustain, Chem. Phar. 37 (2024) 101363.

[21] U. Ceylan, A. Çapan, S.P. Yalçın, M. Sönmez, M. Aygün, Vibrational spectroscopic and thermo dynamical property studies, Fukui functions, HOMO-LUMO, NLO, NBO and crystal structure analysis of a new Schiff base bearing phenoxy-imine group, J. Mol. Struct. 1136 (2017) 222–230, https://doi.org/10.1016/j.molstruc.2017.02.014.

[22] P.G. Cozzi, MetaleSalen Schiff base complexes in catalysis: practical aspects, Chem. Soc. Rev. 33 (2004) 410–421, https://doi.org/10.1039/B307853C.

[23] H. Temel, U. Çakır, H.I. Ugras¸, M. Sekerci, The synthesis, characterization and conductance studıes of new Cu(II), Ni(II) and Zn(II) complexes with the Schiff base derived from 1,2-bis-(o-Aminophenoxy)ethane and salicylaldehyde, J. Coord. Chem. 56 (2003) 943–951, https://doi.org/10.1080/0095897031000135324.

[24] D. Jian-Qin, L. Hong, L. Xue-Chun, C. Xing, C. Jian-Xin, Z. Zhi-Chun, A novel phenoxyimine-based Schiff base ligand and its mononuclear nickel(II) complex: synthesis, crystal structure, norbornene polymerization and catalytic activity, Chin. J. Struct. Chem. 35 (2016) 559–565, https://doi.org/10.14102/j.cnki.0254-5861.2011-0932.

[25] R. Sankar, T.M. Sharmila, 3-Phenoxybenzaldehyde and glycine-derived schiff base M(II) complexes: synthesis, molecular modeling, spectroscopic exploration, and antimicrobial evaluation, Inorg. Chem. Commun. 162 (2024) 112253, https://doi.org/10.1016/j.inoche.2024.112253.

[26] M. Durgun, U. Ceylan, S.P. Yalçun, H. Türkmen, N. Ozdemir, I. Koyuncu, Synthesis, molecular structure, spectroscopic characterization, NBO, NLO and NPA analysis and in vitro cytotoxicity study of 3-chloro-N-(4-sulfamoylphenethyl) propanamide with experimental and computational study, J. Mol. Struct. 1114 (2016) 95–107, https://doi.org/10.1016/j.molstruc.2016.02.062.

[27] H. Şenol, M. Ghaffari-Moghaddam, G.O.A. Toraman, U. Güller, Novel chalcone derivatives of ursolic acid as acetylcholinesterase inhibitors: synthesis, characterization, biological activity, ADME prediction, molecular docking and molecular dynamics studies, J. Mol. Struct. 1295 (2024) 136804, https://doi.org/10.1016/j.molstruc.2023.136804.

[28] M. Karplus, J.A. McCammon, Molecular dynamics simulations of biomolecules, Nat. Struct. Biol. 9 (2002) 646–652, https://doi.org/10.1038/nsb0902-646.

[29] B. Krishnakumar, R. Velmurugan, M. Swaminathan, TiO_2–SO_4^{2-} as a novel solid acid catalyst for highly efficient, solvent free and easy synthesis of chalcones under microwave irradiation, Catal. Commun. 12 (2011) 375–379, https://doi.org/10.1016/j.catcom.2010.10.015.

[30] T.K.R. Dennington, J. Millam, Gauss View, Version 5, Semichem Inc., Shawnee Mission, 2009.

[31] M. Frisch, G. Trucks, H. Schlegel, G. Scuseria, M. Robb, J. Cheeseman, G. Scalmani, V. Barone, B. Mennucci, G. Petersson, H. Nakatsuji, M. Caricato, X. Li, H. Hratchian, A. Izmaylov, J. Bloino, G. Zheng, J. Sonnenberg, M. Hada, D. Fox, Gaussian 09 (Revision A02), Gaussian Inc., Wallingford CT, 2009.

[32] R. Muthukumar, M. Karnan, N. Elangovan, M. Karunanidhi, V. Sankarapandian, K. Venkateswaran, Synthesis, experimental antimicrobial activity, theoretical vibrational analysis, quantum chemical modeling and molecular docking studies of (*E*)-4-(benzylideneamino) benzenesulfonamide, J. Mol. Struct. 1263 (2022) 133187, https://doi.org/10.1016/j.molstruc.2022.133187.

[33] N. Saghdani, A. El Abbouchi, N. El Brahmi, A. Idir, K.O. Rachedi, M. Berredjem, R. Haloui, S. Elkhattabi, H.A. Mouse, T.B. Hadda, M. Bousmina, Design, synthesis, *in-vitro, in-silico*, DFT and POM studies of a novel family of sulfonamides as potent anti-triple-negative breast cancer agents, Comput. Biol. Chem. 113 (2024) 108214, https://doi.org/10.1016/j.compbiolchem.2024.108214.

[34] A.W. Bauer, W.M.M. Kirby, J.C. Sherris, M. Turck, Antibiotic susceptibility testing by a standardized single disk method, Am. J. Clin. Pathol. 45 (1966) 493–496, https://doi.org/10.1093/ajcp/45.4_ts.493.

[35] X.H. Lina, X.J. Yina, J.Y. Liua, S.F.Y. Lia, Elucidation of structures of surface sulfate species on sulfated titania and mechanism of improved activity, Appl. Catal. B: Environ. 203 (2017) 731–739, https://doi.org/10.1016/j.apcatb.2016.10.068.

[36] S.M. Patil, S.A. Vanalakar, S.A. Sankpal, S.P. Deshmukh, S.D. Delekar, Sulfated TiO_2/SnO_2 nanocomposite as a green heterogeneous catalyst for direct amide formation reaction, Result. Chem. 3 (2021) 100102, https://doi.org/10.1016/j.rechem.2021.100102.

[37] S. Bakardjieva, J. Subrt, V. Stengl, M.J. Dianez, M.J. Sayagues, Photoactivity of anatase–rutile TiO_2 nanocrystalline mixtures obtained by heat treatment of homogeneously precipitated anatase, Appl. Catal. B: Environ. 58 (2005) 193–202.

[38] N.D. Kumar, P. Mayavel, I. Muthuvel, G. Thirunarayanan, Solvent-free synthesis, spectral, crystal study and DFT calculations of (*E*)-1-benzyl-*N*-(4-fluorobenzylidene) piperidin-4-amine and (*E*)-1-benzyl-*N*-(naphthalen-2-ylmethylene) piperidin-4-amine, Chem. Data Collect. 30 (2020) 100547, https://doi.org/10.1016/j.cdc.2020.100547.

[39] N. Dege, A.S. Aydın, E. Agar, S. Kansız, S. JoseKavitha, K. BalaSubramani, M. Hemamalini, V. Rajakannan, Synthesis, crystal structure, Hirshfeld surface analysis, *In-Silico* assessment of druggability and molecular docking studies of Schiff base compound, Chem. Data Coll. 25 (2020) 100320, https://doi.org/10.1016/j.cdc.2019.100320.

[40] A. Madani, A. Hellal, D. Aggoun, O. Mokhnache, E. Bentouhami, L. Sibous, Synthesis, crystal structure, Hirshfeld surfaces analysis and electrochemical properties determination of new Schiff base derived from benzidine, J. Mol. Struct. 1304 (2024) 137648, https://doi.org/10.1016/j.molstruc.2024.137648.

[41] M. Asad, M.N. Arshad, A.M. Asiri, H.M. Marwani, K.A. Alamry, M.M. Alam, S. Nazreen, A.A. Elhenawy, M.M. Rahman, Synthesis of *N*-acylated pyrazolines: spectroscopic, crystallographic, Hirshfeld surface, lead sensing and theoretical studies, J. Mol. Liq. 385 (2023) 122340, https://doi.org/10.1016/j.molliq.2023.122340.

[42] N.D. Kumar, M. Swaminathan, K. Selvakumar, M. Durai, I. Muthuvel, H. Ebaid, K. Balu, Y.-H. Ahn, G. Thirunarayanan, $ZnFe_2O_4$ assisted facile green synthesis, structural conformation, *in-silico* and *in-vitro* antimicrobial exploration of some piperidine moiety Schiff's bases, J. Mol. Struct. 1325 (2025) 140918, https://doi.org/10.1016/j.molstruc.2024.140918.

[43] M. Bhatia, An overview of conceptual-DFT based insights into global chemical reactivity of volatile sulfur compounds (VSCs), Comput. Toxicol. 29 (2024) 100295, https://doi.org/10.1016/j.comtox.2023.100295.

[44] K. Ranganathan, M. Subramaniyan, T. Kamatchi, S. Shreedevi, Research design, evaluation, and in vitro assessment of N'-(thiophene-2-carbonyl) pyridine-4-carbohydrazide as a biological agent, J. Mol. Struct. 1322 (2025) 140310, https://doi.org/10.1016/j.molstruc.2024.140310.

[45] S. Azhagiri, S. Jayakumar, S. Gunasekaran, S. Srinivasan, Molecular structure, Mulliken charge, frontier molecular orbital and first hyperpolarizability analysis on 2-nitroaniline and 4-methoxy-2-nitroaniline using density functional theory, Spectrochim. Acta A Mol. Biomol. Spectrosc. 124 (2014) 199–202, https://doi.org/10.1016/j.saa.2013.12.106.

[46] N. Thirughanasambantham, V. Balachandran, B. Narayana, C. Sivakumar, A. Jayashree, M. Kavimani, Pharmaceutical investigation of 2-amino-4-(2-fluoro-phenyl)-5, 10-dioxo-5, 10-dihydro-4H-benzo [g] chromene-3-carbonitrile via computational studies, Inorg. Chem. Commun. 159 (2024) 111709, https://doi.org/10.1016/j.inoche.2023.111709.

[47] O. Trott, A.J. Olson, AutoDock Vina: improving the speed and accuracy of docking with a new scoring function, efficient optiization and multithreading, J. Comput. Chem. 31 (2010) 455–461, https://doi.org/10.1002/jcc.21334.

[48] S. De Falco, The discovery of placental growth factor and its biological activity, Exp. Mol. Med. 44 (20120) 1–9. https://doi.org/10.3858/emm.2012.44.1.025.

[49] A. Daina, O. Michielin, V. Zoete, SwissADME: a free web tool to evaluate pharmacokinetics, drug-likeness and medicinal chemistry friendliness of small molecules, Sci. Rep. 7 (2017) 42717.

[50] R. Subramaniyan, R. Ramarajan, A. Ramalingam, S. Sambandam, A. Petersamy, A. R. Guerroudj, N. Boukabcha, A. Chouaih, Microwave-assisted synthesis, vibrational spectra, Hirshfeld surface and interaction energy, DFT, topology, in silico ADMET and molecular docking studies of 1,2-bis(4-Microwave-assistedmethoxybenzylidene)hydrazine, J. Mol. Struct. 1278 (2023) 134946, https://doi.org/10.1016/j.molstruc.2023.134946.